Understanding the Impact of Contact-Induced Strain on the Electrical Performance of Monolayer WS$_2$ Transistors

Lauren Hoang, Marc Jaikissoon, Çağıl Köroğlu, Zhepeng Zhang, Robert K. A. Bennett, Jung-Hwan Song, Jerry A. Yang, Jung-Soo Ko, Mark L. Brongersma, Krishna C. Saraswat, Eric Pop, and Andrew J. Mannix*

ACCESS | 📊 Metrics & More | 📄 Article Recommendations | 🆂🅸 Supporting Information

ABSTRACT: Two-dimensional (2D) electronics require low contact resistance (R_C) to approach their fundamental limits. WS$_2$ is a promising 2D semiconductor that is often paired with Ni contacts, but their operation is not well understood considering the nonideal alignment between the Ni work function and the WS$_2$ conduction band. Here, we investigate the effects of contact size on nanoscale monolayer WS$_2$ transistors and uncover that Ni contacts impart stress, which affects the WS$_2$ device performance. The strain applied to the WS$_2$ depends on contact size, where long (1 μm) contacts ($R_C \approx 1.7$ k$\Omega \cdot \mu$m) show a 78% reduction in R_C compared to shorter (0.1 μm) contacts ($R_C \approx 7.8$ k$\Omega \cdot \mu$m). We also find that thermal annealing can relax the WS$_2$ strain in long-contact devices, increasing R_C to 8.5

Contact size (L_C) influences strain in WS$_2$ devices

k$\Omega \cdot \mu$m. These results reveal that thermo-mechanical phenomena can significantly influence 2D semiconductor−metal contacts, presenting opportunities to optimize device performance through nanofabrication and thermal budget.

KEYWORDS: 2D transistors, strain engineering, contact resistance, thermal annealing
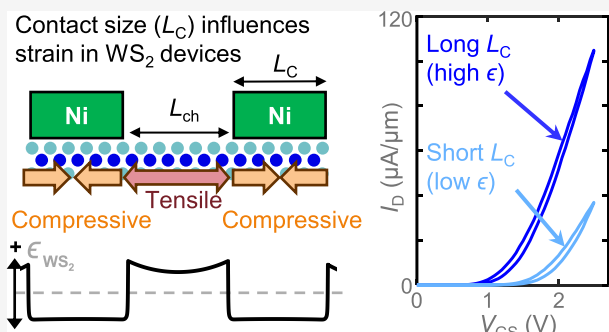
Two-dimensional (2D) semiconductors, such as transition metal dichalcogenides (TMDs), have gained significant interest for next-generation electronics due to their atomically thin nature and good charge mobility in subnanometer films.[1,2] Monolayer tungsten disulfide (WS$_2$) has one of the highest predicted mobilities and largest band gaps of the TMDs, potentially enabling good low-power performance.[3−5] However, further advances are limited by the high electrical contact resistance (R_C) to WS$_2$-based field-effect transistors (FETs).[6] Several techniques have been shown to reduce the R_C to *n*-type TMDs, such as depositing semimetals (e.g., Bi and Sb),[7−9] using low melting point metals (e.g., In and Sn),[10,11] or transferred contacts,[12] although many of these approaches are not considered industry-compatible. Furthermore, *n*-type contacts to WS$_2$ lag behind MoS$_2$ and more efforts are needed to investigate performance at reduced, submicron dimensions.

In principle, the R_C at the metal−semiconductor interface depends on: (1) the metal−semiconductor energy band alignment (including Fermi level pinning), where the metal work function (ϕ_m) influences the Schottky contact barrier, and (2) the number of defects created during metal deposition, which tends to increase with the metal's melting point[11] or reactivity,[13,14] thus causing additional Fermi level pinning. Nickel (Ni) is often used as the metal contact to *n*-type WS$_2$,[15−19] with the lowest reported R_C for Ni falling below 1 k$\Omega \cdot \mu$m at room temperature.[16] In our devices, we find that Ni (Figure 1a, b) exhibits the lowest R_C compared to other metals

such as Au, In, Sb (Figure S1). However, the origin of the low R_C for Ni on WS$_2$ is not well understood and is in fact counterintuitive for two reasons: (1) Ni has a large work function ($\phi_{Ni} \approx 5.15$ eV),[20] which is not well aligned to the conduction band of monolayer WS$_2$ (Figure 1c); and (2) the high melting point of Ni (1455 °C) suggests that Ni contacts could produce more defects in the WS$_2$ during physical vapor deposition.[20,21]

In contrast to the well-studied impact of metal work function alignment and metal-induced gap states upon R_C, the mechanical effects of contacts are relatively underexplored. Thin metal films often contain high amounts of residual stress upon deposition, especially Ni.[22,23] The band structure of 2D semiconductors is known to be sensitive to strain,[24,25] and tensile strain has been recently shown to increase the electron mobility of monolayer MoS$_2$ and WS$_2$.[26−30] Strain can be imparted by bending the substrate,[26−28] by a capping layer,[29−33] or at the contacts.[34,35] In addition, the stress in such thin films can be modified by thermal treatment,[36] which may impact the overall thermal budget for 2D transistor
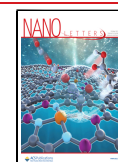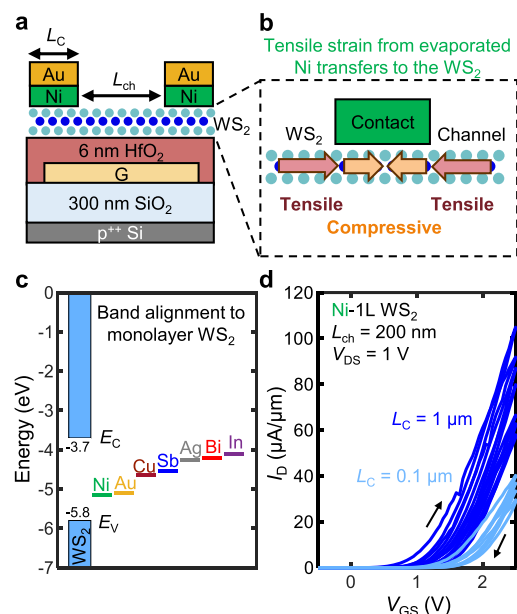
Figure 1. (a) Schematic of our monolayer (1L) WS$_2$ devices on local back-gates with thin HfO$_2$ and Ni contacts capped with Au. (b) Zoomed-in view of schematic in (a), showing strain in WS$_2$ from Ni deposition. (c) The band gap of monolayer WS$_2$ in approximate relation to the work function (ϕ_m) of some bulk metals and semimetals. E_C denotes the conduction band edge and E_V denotes the valence band edge of 1L WS$_2$. (d) Measured I_D vs V_{GS} curves for all L_{ch} = 200 nm devices with L_C = 1 μm (8 devices) and L_C = 0.1 μm (4 devices), showing clear I_D improvement with long contacts. Arrows denote the voltage sweep direction, showing clockwise hysteresis.

fabrication. Therefore, it is necessary to explore the potential role of strain in contact engineering, especially when depositing highly stressed metals like Ni (Figure 1a,b).[35]

In this work, we uncover the important role that strain plays at the Ni−WS$_2$ interface and how it impacts the device transconductance ($g_m = \partial I_D/\partial V_{GS}$) and R_C. We observe that electron-beam deposited Ni applies high tensile stresses to the WS$_2$ channel (Figure 1b). These stresses are approximately proportional to the contact length (L_C), leading to ~2.64× increase in on-state current with long contacts (L_C = 1 μm) compared to short contacts (L_C = 0.1 μm) for a channel length (L_{ch}) of 50 nm (and ~1.37× increase at L_{ch} = 1 μm). Long contacts also create significant strain near the WS$_2$ contact region, resulting in 78% lower R_C. However, we observe that thermal annealing causes relaxation of the strain in unencapsulated devices, resulting in nearly identical values of R_C for both long and short contact devices post-annealing. These observations highlight new strategies to boost device performance and emphasize the critical role of thermo-mechanical effects in evaluating different contact materials.

We studied monolayer WS$_2$ devices in several geometries, predominantly using local back-gates with a low equivalent oxide thickness (EOT) insulator (see Methods). The local back-gates (Figure 1a) are patterned by lift-off from 2 nm/8 nm Ti/Pt (Pt on top) followed by thermal atomic layer deposition of 6 nm HfO$_2$. The WS$_2$ was grown separately on sapphire[37] and transferred onto HfO$_2$. WS$_2$ channels were patterned by XeF$_2$ etching, and transfer length method (TLM) structures with L_{ch} from 30 nm to 1 μm were defined using electron beam (e-beam) lithography. Ni (15 nm) capped with Au (20 nm) was deposited via e-beam evaporation at ~10^{-8}

Torr to form the contacts. The Ni/Au thin film exhibits a total stress of 160−175 MPa (Table S1). Electrical measurements were performed at 296 K under vacuum (~10^{-4} Torr).

Because the stress applied by the contact increases with L_C,[31,35] contacts with L_C values of 0.1 and 1 μm were patterned to examine the effect of contact-applied stress on the device performance. As discussed later, the short L_C (0.1 μm) is more than twice as long as the current transfer length, indicating that current crowding should not affect device behavior. Figure 1d shows a comparison of measured transfer (I_D vs V_{GS}) curves at L_{ch} = 200 nm between the short (L_C = 0.1 μm) and long (L_C = 1 μm) contact devices. Devices with longer contacts have higher drain current, more negative threshold voltage (V_T), and increased g_m. For such devices with L_{ch} = 200 nm, we find that increasing L_C (0.1 to 1 μm) doubles the median $I_{D,max}$ (defined as the largest drain current I_D over the V_{GS} range applied) from 35.1 μA/μm to 70.2 μA/μm, shifts the median V_T negatively by −0.1 V (from 0.9 to 0.8 V), and increases the median peak g_m from 32.7 μS/μm to 54.3 μS/μm, at V_{DS} = 1 V.

To understand these changes, we performed finite-element analysis method simulations to reveal the impact of stressed metal contacts on the strain distribution along the WS$_2$ channel, as a function of both L_C and L_{ch}. Figure 2a shows the distribution of in-plane strain in WS$_2$ devices with L_C = 1 μm and various L_{ch}. For a long-channel device (L_{ch} = 1 μm), the tensile strain in the WS$_2$ is highest next to the contact edge and decays toward the center of the channel. As the L_{ch} is reduced, the maximum WS$_2$ tensile strain increases from 0.18% (L_{ch} = 1 μm) to 0.49% (L_{ch} = 30 nm) at the contact edge. The simulations are described in greater detail in Supporting Information Section 3, where it is also shown that the strain in WS$_2$ is predominantly uniaxial, along the direction of current flow.

Figure 2b illustrates the strain in WS$_2$ when L_C is reduced to 0.1 μm. Evidently, the maximum tensile strain is an order of magnitude lower than for L_C = 1 μm, ranging from 0.017% to 0.03% strain. This occurs because the stress in the contacts is determined primarily by the deposition conditions and is therefore independent of the contact geometry. The total (compressive) change in the L_C (the amount by which the contacts pull on the channel) is approximately proportional to the nominal L_C. Thus, we find that both L_{ch} and L_C can significantly affect the tensile strain in the WS$_2$ channel. The ratio between L_{ch} and L_C will dictate the overall strain profile: even at short L_C, the strain in the channel will increase as L_{ch} is scaled down.

We used photoluminescence (PL) spectroscopy to validate the WS$_2$ strain profile along the channel (see Supporting Information Section 4). Because tensile strain in WS$_2$ reduces the direct band gap by lowering the conduction band, the PL peak is known to redshift with tensile strain.[38−40] To probe the strain distribution in WS$_2$ away from a contact edge, we map PL spectra along the WS$_2$ with a pixel spacing of 200 nm. Figure 2c displays an optical image and the integrated intensity in the range 1.7−2.2 eV, to accurately determine the contact location (dark blue). Test devices were fabricated on 100 nm SiO$_2$ (on Si) instead of metal local back-gates to accurately map the confocal PL response. The PL spectrum is fitted (with a weighted Gaussian−Lorentzian line shape) and the neutral A exciton peak is plotted with respect to the distance from the contact edge (Figure 2d). The A exciton peak of WS$_2$ close to the contact edge is lowered by 20 meV, consistent with ~0.5%
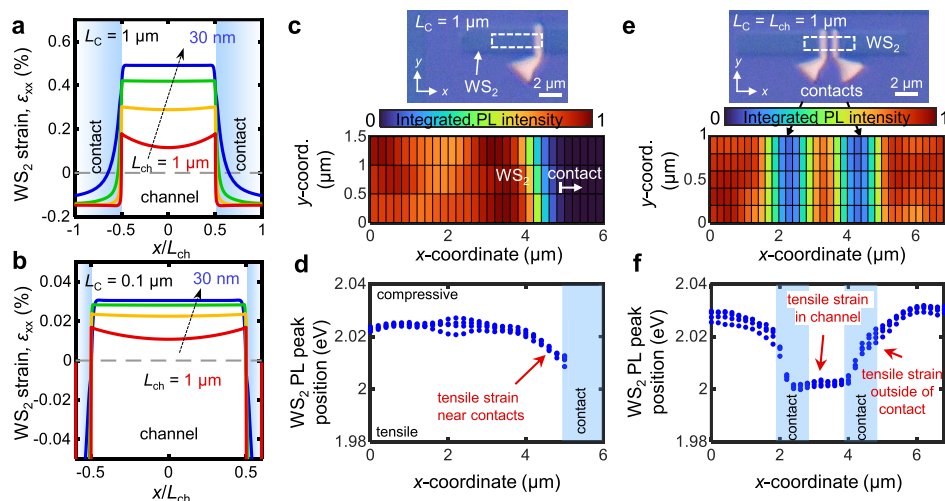
Figure 2. (a) Simulated horizontal strain profile along a device with contact length, $L_C = 1$ μm and channel length, $L_{ch} = 1$ μm, 300 nm, 100 nm, and 30 nm. The position x is normalized by L_{ch}, for easier visualization. (b) Simulated horizontal strain profile along a device with $L_C = 0.1$ μm and $L_{ch} = 1$ μm, 300 nm, 100 nm, and 30 nm. (c) Integrated photoluminescence (PL) spectral intensity map away from a contact edge (on the right). (d) Measured A exciton peak in WS$_2$ as a function of x-coordinate, for the map in (c). (e) Integrated PL spectral intensity map of a device with L_{ch} = 1 μm and $L_C = 1$ μm, demonstrating the position of the contacts (dark blue). (f) Measured A exciton peak of WS$_2$ as a function of x-coordinate, for the map in (e). For panels (d, f), we note that the data plotted under the contact regions represent regions of WS$_2$ just outside the contact edge due to the finite laser spot size ($\sim$500 nm). WS$_2$ directly under the contact cannot be probed due to the metal layers on top.

tensile strain based on previous experimental work.[40] The WS$_2$ PL peak position reverts to its nominal value $\sim$1.5 μm away from the contact edge, illustrating an upper bound for the lateral decay length of the strain imparted by the stressed metal on WS$_2$.[33] We note that these measurements are constrained by the diffraction limit and PL cannot probe the WS$_2$ under the metal contact. The signal arising from the nominal contact regions is due to the finite laser spot size, which collects some signal from the region outside the contacts.

We also performed PL mapping of a device with $L_{ch} = 1$ μm and $L_C = 1$ μm in Figure 2e,f. The PL peak in the channel is 30 meV lower than the nominal PL peak, corresponding to $\sim$0.7% strain induced in the material.[40] The profile of the A exciton peak position in Figure 2f matches the expected strain profile obtained by simulations in Figure 2a both within the channel and outside the contacts, supporting our conclusion that the metal contacts induce strain in the WS$_2$ (Figure S4a, b).

As seen in Figure 1d, the g_m and I_D are both strongly dependent on the contact and channel dimensions. The measured transfer curves in Figure 3a,b compare long contact ($L_C = 1$ μm) and short contact ($L_C = 0.1$ μm) devices for $L_{ch} = 1$ μm and 50 nm, respectively. At all L_{ch}, we consistently observe that long contacts demonstrate higher $I_{D,max}$. For the long-channels ($L_{ch} = 1$ μm), the on-state current (I_{on}) at fixed overdrive voltage ($V_{ov} = V_{GS} - V_T$) of 1.1 V has a median increase of 1.35× when switching from $L_C = 0.1$ μm to $L_C = 1$ μm (Figure 3a, c). In contrast, for short-channels ($L_{ch} = 100$ nm), the long-contact devices show a 2.67× increase in I_{on} (Figure 3b, c). Figure 3c summarizes the strong impact of L_C on the nonlinear relationship between I_{on} (at $V_{ov} = 1.1$ V) and L_{ch}: namely, shorter channels display a greater increase of I_{on} when they have long contacts. This is consistent with the simulations in Figure 2a, where shorter channel devices exhibit a larger tensile strain in the WS$_2$. Figure 3d plots the experimentally measured median peak g_m at each L_{ch}, showing a clear increase in peak g_m for devices with long contacts. When L_{ch} is long ($L_{ch} = 1$ μm) the median peak g_m increases by 1.74× for the long contacts (i.e., higher strain). In devices with long

L_{ch}, which are dominated by the channel resistance R_{ch} (e.g., $R_{ch} > 10$ R_C), it is reasonable to expect that g_m is mostly influenced by mobility.[41] Thus, the increase in g_m is attributed to an increase in mobility in this long channel regime. This is consistent with recent studies which have found tensile strain to reduce intervalley scattering in the conduction band of monolayer MoS$_2$ or WS$_2$, leading to higher mobility.[26−29]

From our TLM structures, we also estimate the R_C with the two L_C values (Figure 3e), finding that long contacts lead to substantially lower R_C than short contacts. The longer L_C yields an R_C of 1.73 k$\Omega\cdot\mu$m at $V_{ov} = 2.3$ V for our best TLM structure. This is consistent with some of the best existing Ni contacts to monolayer WS$_2$ in the literature, which range between 0.72 to 2.6 k$\Omega\cdot\mu$m (see Table S3).[15,18,42] In terms of their nominal contact structure, these studies are equivalent to our "strained" long contact case, with Ni thicknesses >15 nm and L_C on the order of 1 μm. We note that the TLM extraction method for R_C assumes the same sheet resistance for all L_{ch}, but this may exhibit some dependence on strain. However, ensuring the TLM data are taken at the same V_{ov} and having short channel devices (here, $L_{ch} < 100$ nm) in the TLM appears sufficient to estimate R_C, because the short-channel devices are almost entirely contact-limited.

In contrast to the long contacts, our short contacts have R_C of 7.8 k$\Omega\cdot\mu$m at $V_{ov} = 1.8$ V. We note that our short L_C (0.1 μm) is comfortably greater than the estimated transfer length, $L_T \approx 37$ nm (Supporting Information Section 6), indicating that the higher R_C is not due to current crowding,[2] but is instead a result of the lower WS$_2$ strain with the shorter contacts. The improvement in R_C likely stems from the higher concentration of electrons in the region next to the contacts. The high tensile strain near the contacts (Figure 2a) lowers the conduction band, increasing the electron concentration. Long contact devices also have lower V_T (by −0.27 V) (Figure S10b), which is consistent with greater tensile strain in the WS$_2$ channel, lowering the conduction band edge and increasing the electron density in the channel and contacts. We can see that the difference in L_C significantly affects both
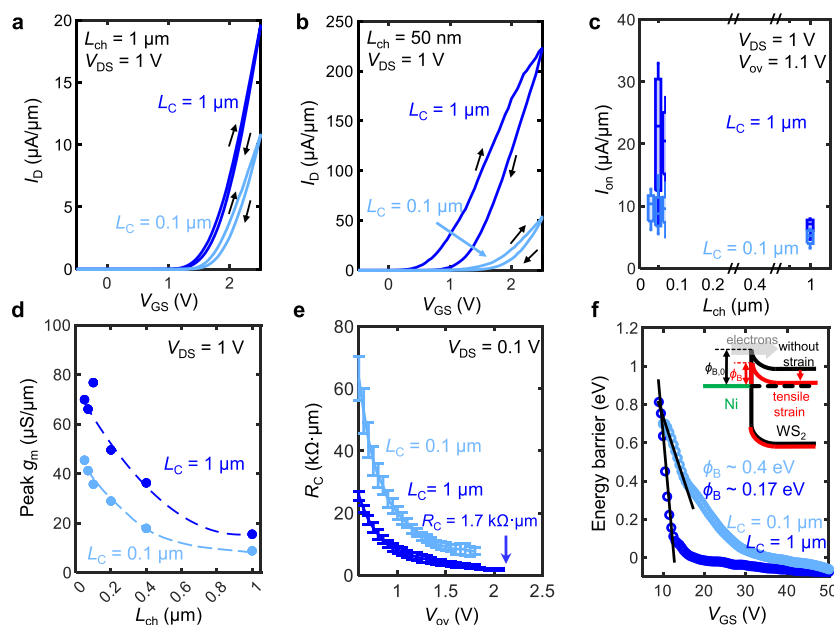
Figure 3. (a) I_D vs V_{GS} curves of a L_C = 1 μm and L_C = 0.1 μm device with L_{ch} = 1 μm. Arrows denote the voltage sweep direction, showing clockwise hysteresis. (b) I_D vs V_{GS} curves of a L_C = 1 μm and L_C = 0.1 μm device with L_{ch} = 50 nm. (c) On-state current (I_{on}) at a fixed overdrive V_{ov} = 1.1 V versus L_{ch}, comparing a total of 103 devices with L_C = 1 μm and L_C = 0.1 μm. (d) Peak transconductance (g_m) vs L_{ch} for L_C = 1 μm and L_C = 0.1 μm, plotting the median device at each L_{ch}. The dashed blue lines are qualitative guides to highlight the trend. (e) Estimated R_C for L_C = 1 μm and L_C = 0.1 μm, showing ~5× reduction in R_C with long contacts (fitting the highest performing TLM). (f) Electron Schottky barrier height analysis for long contact and short contact devices, demonstrating a large decrease in barrier height (ϕ_B) for long contact devices. Inset: Schematic of energy band diagram with strain experienced at the channel and near contacts.

R_{ch} and R_C, with long contacts increasing g_m by 1.74× (which we attribute to enhanced mobility) and decreasing R_C by 78%.

Tensile strain in TMDs like WS$_2$ lowers the conduction band edge,[27,43] decreasing the Schottky barrier height (SBH) for electron injection at the contacts.[24,44,45] We quantified the impact of contact-induced strain on SBH for the long (L_C = 1 μm) and short (L_C = 0.1 μm) contacts (Figure 3f), using temperature-dependent measurements (Figures S11, S12). The SBH decreases from $\phi_B \approx$ 400 meV for short contacts to $\phi_B \approx$ 170 meV for long contacts with greater strain (for the single devices plotted in Figure 3f). Comparing measurements for three long and three short contact devices reveals an average barrier height reduction of 170 meV from the strain induced by the long contacts. This substantial reduction illustrates that strain can modify the effective SBH at metal–2D interfaces independently from the metal work function. This dependence of R_C on strain and contact dimensions is often overlooked and may directly affect the apparent performance of various contacts reported in the literature. We expect these results to be qualitatively similar to other TMDs[25] such as MoS$_2$[27,35] and WSe$_2$[45] due to their improvement in electron mobility with tensile strain.

Thermal processing is known to affect thin film stress and thus is expected to change the strain profile and electrical transport of the WS$_2$ transistors. We investigate the impact of a 150 °C, 2-hour vacuum anneal on the Ni–WS$_2$ device performance with respect to L_C and L_{ch}. After annealing, the highly strained long contact devices (L_C = 1 μm) show decreased I_{on}, an effect which is especially apparent for the short channel devices (Figure 4a, c). In contrast, the devices with short contacts (lower initial strain) showed negligible change in performance after annealing (Figure 4b, c). The largest decrease in I_{on} after annealing occurs for devices with

long contacts and short channels (Figure 4c). Additionally, for the higher-strained, long-contact devices, annealing decreases the peak g_m from 17.1 μS/μm to 14.5 μS/μm for L_{ch} = 1 μm. This decrease in peak g_m for long channel devices is consistent with a loss of strain-induced mobility enhancement in the WS$_2$ channel after annealing.

Figure 4d shows the increase in the *median* R_C due to annealing, for both the long contact devices (3.8 k$\Omega\cdot\mu$m to 14.1 k$\Omega\cdot\mu$m) and short contact devices (9.5 k$\Omega\cdot\mu$m to 14.1 k$\Omega\cdot\mu$m), at V_{ov} = 1.75 V. Thus, the value of R_C for long contact devices increased by ~3.7× while the short contacts increased by only ~1.5 ×. Furthermore, the final R_C after annealing for both the long contact and short contact devices are similar, both with a median TLM fit of 14.1 k$\Omega\cdot\mu$m at V_{ov} = 1.75 V. This suggests that the electrical properties of the WS$_2$/Ni interface are rendered more similar following annealing. Evidently, the performance boost from strain induced by the long contacts is lost after annealing, which further supports the conclusion that strain is responsible for the improved R_C and g_m. This also suggests that the relatively mild annealing condition of 150 °C is above the thermal budget for this combination of contact geometry and stress state in unencapsulated devices. However, the significant improvement in electronic properties provides strong motivation to preserve strain after annealing. We observe that encapsulating the devices with AlO$_x$ successfully maintains the strain from the L_C = 1 μm contacts after annealing (Figure S13).

Our device observations are consistent with in-plane X-ray diffraction (XRD) analysis, which reveals changes in Ni/Au strain upon annealing (Figure S14). The Ni layer initially exhibited in-plane tensile strain (0.137%) which increased to 0.174% after annealing. Likewise, the initial compressive strain in the Au layer (−0.241%) was reduced after annealing
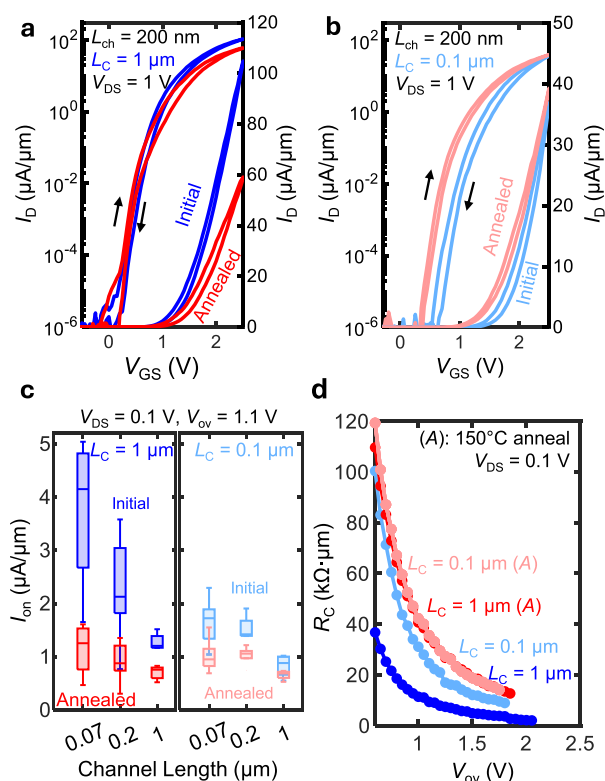
Figure 4. Contact length-dependent annealing effect on device performance. (a) Current vs gate voltage (V_{DS} = 1 V) of a L_C = 1 μm device before and after a 150 °C vacuum anneal. Arrows denote the voltage sweep direction, showing small clockwise hysteresis. (b) Current vs gate voltage (V_{DS} = 1 V) of a L_C = 0.1 μm device before and after a 150 °C vacuum anneal. (c) On-state current at a fixed overdrive V_{ov} = 1.1 V vs L_{ch} before and after annealing, for L_C = 1 μm (left) and L_C = 0.1 μm (right). Short channel, long contact devices show largest decrease in current. (d) *Median* R_C for L_C = 1 μm and L_C = 0.1 μm before and after annealing.

(−0.127%). This net increase in tensile strain within the contact metals imparts a large stress to the WS_2, causing the WS_2 to exceed the traction limit and relax by slipping freely on HfO_2.[33] This aligns with simulation results in Figure S3, where weak mechanical coupling between the WS_2 and HfO_2 results in low strain in the WS_2 channel.

We have considered other potential mechanisms that could explain the increase in R_C with annealing, such as diffusion[46] or interfacial reactions.[14,47] Ni has been shown to diffuse into MoS_2 and increase R_C following annealing at 250−400 °C.[46] Additionally, the oxidation of Ni has been proposed to explain increased R_C with annealing.[2] However, these mechanisms do not account for the observation that the largest decrease in I_{on} occurs in the most highly strained devices (long contacts, short channel). Thus, we attribute the increased R_C after annealing to strain relaxation in the WS_2.

In conclusion, we uncover that electron-beam evaporated Ni contacts impart tensile strain in a monolayer WS_2 channel, ultimately reducing the R_C. The effects of tensile stress in the Ni contact can be comparable in magnitude to the contributions from the work function and the metal−2D interfacial quality. WS_2 devices with long contacts (1 μm) have a best (median) R_C of 1.73 (2.00) k$\Omega\cdot\mu$m which worsens for short (0.1 μm) contacts to 7.8 (8.9) k$\Omega\cdot\mu$m. We also demonstrate that thermal annealing affects contact-induced strain, which depends on the contact length, L_C.

Considering the key role of R_C as a limiting factor in device performance and the numerous recent studies of contacts in 2D transistors, these results highlight the importance of carefully examining metal strain effects to determine the origin of changes in R_C. This is especially important when considering the implications for L_C scaling: many contemporary studies use contacts long enough to cause strain effects, yet future nanoscale devices must use short contacts. The sensitivity of R_C and mobility to annealing conditions, resulting from strain relaxation, also suggests that strict attention to thermal budget or strain stabilization is required.

■ METHODS

WS_2 Growth. Monolayer WS_2 was grown on SiO_2/Si substrates and sapphire by chemical vapor deposition (CVD) using diethyl sulfide (DES) and ammonium metatungstate (AMT) precursors.[37] 0.6 g AMT and 0.1 g potassium hydroxide were dissolved in 30 mL deionized water and dip-coated on the edges of the substrate. For the sapphire (SiO_2) substrate, the substrate is annealed in the furnace at 775 °C for 6 h with a DES flow rate of 0.05 sccm (0.12 sccm). N_2 and H_2 were used as carrier gases during the growth. Representative Raman and PL spectra of the WS_2 films are shown in a previous study by Zhang et al.[37]

Device Fabrication and Electrical Measurements. Monolayer WS_2 was grown on sapphire and then transferred onto local back-gates covered by 6 nm HfO_2. Device fabrication and transfer details have been described in depth previously.[48] In summary, the local back gates were defined by lift-off of 2 nm/8 nm Ti/Pt followed by the HfO_2 gate dielectric by thermal atomic layer deposition at 200 °C. Coarse contact pads were then defined by lift-off of 2/20 nm Ti/Pt. Polystyrene (PS) was spin-coated on top of the WS_2 and then transferred using NaOH, with thorough rinsing in DI water. An O_2 plasma treatment (100 W, 1 min) of the HfO_2 dielectric was done before transferring the PS/WS_2 film to modify the substrate's surface energy. PS was removed in toluene, then a vacuum anneal (200 °C, 2 h, ~10^{-6} Torr) was performed to promote adhesion. After the transfer, channel definition was done using XeF_2 etching. Electron beam lithography was used to pattern the fine contacts. Ni/Au (15/20 nm) were e-beam evaporated at ~10^{-8} Torr. Electrical measurements were performed at 296 K in a Janis ST-100 vacuum probe station at ~10^{-4} Torr, using a Keithley 4200 semiconductor parameter analyzer.

For contact resistance (R_C) extraction, the transfer length method (TLM) was used. In a two-terminal device, the major components are the R_C and the channel resistance (R_{ch}). The total resistance in k$\Omega\cdot\mu$m (normalized by the channel width) can be expressed as $R_{TOT} = 2R_C + R_{ch} = 2R_C + R_{sh}L_{ch}$, where R_{sh} is the sheet resistance of the channel. The R_C is evaluated by plotting R_{TOT} versus L_{ch} and the y-intercept at $L_{ch} = 0$ gives the resultant $2R_C$. The R_C is extracted for each gate overdrive $V_{ov} = V_{GS} - V_T$, with V_T from the constant-current method at $I_D = 10^{-2} \mu$A/μm.[49]

■ ASSOCIATED CONTENT

ⓈI Supporting Information

The Supporting Information is available free of charge at https://pubs.acs.org/doi/10.1021/acs.nanolett.4c02616.

Device fabrication process, stress characterization, finite element analysis information, photoluminescence spec-

troscopy measurement and peak fitting, literature benchmarking, transfer length determination, transconductance threshold voltage extractions, Schottky barrier height extraction, density functional theory simulations, effect of annealing on Ni−WS$_2$ devices on SiO$_2$, and X-ray diffraction (PDF)

■ AUTHOR INFORMATION

Corresponding Author

Andrew J. Mannix − *Department of Materials Science & Engineering, Stanford University, Stanford, California 94305, United States; Stanford Institute for Materials and Energy Sciences, SLAC National Accelerator Laboratory, Menlo Park, California 94025, United States;* ◎ orcid.org/0000-0003-4788-1506; Email: ajmannix@stanford.edu

Authors

Lauren Hoang − *Department of Electrical Engineering, Stanford University, Stanford, California 94305, United States;* ◎ orcid.org/0009-0001-7556-8560

Marc Jaikissoon − *Department of Electrical Engineering, Stanford University, Stanford, California 94305, United States;* ◎ orcid.org/0000-0001-5102-6348

Çağıl Köroğlu − *Department of Electrical Engineering, Stanford University, Stanford, California 94305, United States;* ◎ orcid.org/0000-0002-2701-9241

Zhepeng Zhang − *Department of Materials Science & Engineering, Stanford University, Stanford, California 94305, United States;* ◎ orcid.org/0000-0002-9870-0720

Robert K. A. Bennett − *Department of Electrical Engineering, Stanford University, Stanford, California 94305, United States;* ◎ orcid.org/0000-0001-7427-8724

Jung-Hwan Song − *Geballe Laboratory for Advanced Materials, Stanford University, Stanford, California 94305, United States;* ◎ orcid.org/0000-0001-9502-5718

Jerry A. Yang − *Department of Electrical Engineering, Stanford University, Stanford, California 94305, United States;* ◎ orcid.org/0000-0001-5521-8523

Jung-Soo Ko − *Department of Electrical Engineering, Stanford University, Stanford, California 94305, United States;* ◎ orcid.org/0009-0006-1890-9038

Mark L. Brongersma − *Geballe Laboratory for Advanced Materials, Stanford University, Stanford, California 94305, United States*

Krishna C. Saraswat − *Department of Electrical Engineering, Stanford University, Stanford, California 94305, United States; Department of Materials Science & Engineering, Stanford University, Stanford, California 94305, United States*

Eric Pop − *Department of Electrical Engineering, Stanford University, Stanford, California 94305, United States; Department of Materials Science & Engineering and Department of Applied Physics, Stanford University, Stanford, California 94305, United States;* ◎ orcid.org/0000-0003-0436-8534

Complete contact information is available at:
https://pubs.acs.org/10.1021/acs.nanolett.4c02616

Author Contributions

L.H., M.J., and J.-S.K. fabricated the devices under the supervision of A.J.M., E.P., and K.C.S. L.H. conducted the device measurements and analysis with the help of M.J., under A.J.M. and E.P. Z.Z. and L.H. performed the WS$_2$ material growth. Ç.K. performed the finite-element analysis simulations, and R.K.A.B. performed the density functional theory simulations with input from L.H. L.H. performed the PL characterization and analysis with help from J.-H.S. and J.A.Y. The manuscript was written through contributions of all authors. All authors have given approval to the final version of the manuscript.

Notes

The authors declare no competing financial interest.

■ REFERENCES

(1) Chhowalla, M.; Jena, D.; Zhang, H. Two-dimensional semiconductors for transistors. *Nat. Rev. Mater.* **2016**, *1*, 16052.

(2) English, C. D.; Shine, G.; Dorgan, V. E.; Saraswat, K. C.; Pop, E. Improved Contacts to MoS$_2$ Transistors by Ultra-High Vacuum Metal Deposition. *Nano Lett.* **2016**, *16*, 3824−3830.

(3) Su, S.-K.; Chuu, C.-P.; Li, M.-Y.; Cheng, C.-C.; Wong, H.-S. P.; Li, L.-J. Layered Semiconducting 2D Materials for Future Transistor Applications. *Small Struct.* **2021**, *2*, 2000103.

(4) Guo, Y.; Liu, D.; Robertson, J. 3D Behavior of Schottky Barriers of 2D Transition-Metal Dichalcogenides. *ACS Appl. Mater. Interfaces* **2015**, *7*, 25709−25715.

(5) Gilardi, C.; et al. Extended Scale Length Theory for Low-Dimensional Field-Effect Transistors. *IEEE Trans. Electron Devices* **2022**, *69*, 5302−5309.

(6) Wang, Y.; Chhowalla, M. Making clean electrical contacts on 2D transition metal dichalcogenides. *Nat. Rev. Phys.* **2022**, *4*, 101−112.

(7) Shen, P.-C.; et al. Ultralow contact resistance between semimetal and monolayer semiconductors. *Nature* **2021**, *593*, 211−217.

(8) Li, M.-Y. et al. Wafer-Scale Bi-Assisted Semi-Auto Dry Transfer and Fabrication of High-Performance Monolayer CVD WS$_2$ Transistor. In *2022 IEEE Symposium on VLSI Technology and Circuits, VLSI Technology and Circuits*, 2022; pp 290−291.

(9) Li, W.; et al. Approaching the quantum limit in two-dimensional semiconductor contacts. *Nature* **2023**, *613*, 274−279.

(10) Wang, Y.; et al. Van der Waals contacts between three-dimensional metals and two-dimensional semiconductors. *Nature* **2019**, *568*, 70−74.

(11) Kumar, A. et al. Sub-200 Ω·μm Alloyed Contacts to Synthetic Monolayer MoS$_2$. In *2021 IEEE International Electron Devices Meeting (IEDM)*, 2021; pp 7.3.1−7.3.4.

(12) Liu, Y.; Huang, Y.; Duan, X. Van der Waals integration before and beyond two-dimensional materials. *Nature* **2019**, *567*, 323−333.

(13) Schauble, K.; et al. Uncovering the effects of metal contacts on monolayer MoS_2. *ACS Nano* 2020, 14, 14798−14808.

(14) Smyth, C. M.; Addou, R.; Hinkle, C. L.; Wallace, R. M. Origins of Fermi Level Pinning between Tungsten Dichalcogenides (WS_2, WTe_2) and Bulk Metal Contacts: Interface Chemistry and Band Alignment. *J. Phys. Chem. C* 2020, 124, 14550−14563.

(15) Sun, Z.; et al. Statistical Assessment of High-Performance Scaled Double-Gate Transistors from Monolayer WS_2. *ACS Nano* 2022, 16, 14942−14950.

(16) Shi, X.; Li, X.; Guo, Q.; Zeng, M.; Wang, X.; Wu, Y. Ultrashort channel chemical vapor deposited bilayer WS_2 field-effect transistors. *Appl. Phys. Rev.* 2023, 10, 011405.

(17) Li, X.; Shi, X.; Marian, D.; Soriano, D.; Cusati, T.; Iannaccone, G.; Fiori, G.; Guo, Q.; Zhao, W.; Wu, Y. Rhombohedral-stacked bilayer transition metal dichalcogenides for high-performance atomically thin CMOS devices. *Sci. Adv.* 2023, 9, No. eade5706.

(18) Shi, X.; et al. Improved Self-Heating in Short-Channel Monolayer WS_2 Transistors with High-Thermal Conductivity BeO Dielectrics. *Nano Lett.* 2022, 22, 7667−7673.

(19) Pang, C. S.; Wu, P.; Appenzeller, J.; Chen, Z. Thickness-Dependent Study of High-Performance WS_2-FETs with Ultrascaled Channel Lengths. *IEEE Trans. Electron Devices* 2021, 68, 2123−2129.

(20) Michaelson, H. B. The work function of the elements and its periodicity. *J. Appl. Phys.* 1977, 48, 4729−4733.

(21) Yang, N.; et al. Ab Initio Computational Screening and Performance Assessment of van der Waals and Semimetallic Contacts to Monolayer WSe_2 P-Type Field-Effect Transistors. *IEEE Trans. Electron Devices* 2023, 70, 2090−2097.

(22) Floro, J. A.; Chason, E.; Cammarata, R. C.; Srolovitz, D. J. Physical Origins of Intrinsic Stresses in Volmer−Weber Thin Films. *MRS Bull.* 2002, 27, 19−25.

(23) Yu, H. Z.; Thompson, C. V. Correlation of shape changes of grain surfaces and reversible stress evolution during interruptions of polycrystalline film growth. *Appl. Phys. Lett.* 2014, 104, 141913.

(24) Johari, P.; Shenoy, V. B. Tuning the electronic properties of semiconducting transition metal dichalcogenides by applying mechanical strains. *ACS Nano* 2012, 6, 5449−5456.

(25) Hosseini, M.; Elahi, M.; Pourfath, M.; Esseni, D. Strain-induced modulation of electron mobility in single-layer transition metal dichalcogenides MX_2 (M = Mo, W; X = S, Se). *IEEE Trans. Electron Devices* 2015, 62, 3192−3198.

(26) Datye, I. M.; et al. Strain-Enhanced Mobility of Monolayer MoS_2. *Nano Lett.* 2022, 22, 8052−8059.

(27) Yang, J. A.; et al. Biaxial Tensile Strain Enhances Electron Mobility of Monolayer Transition Metal Dichalcogenides. *ACS Nano* 2024, 18, 18151−18159.

(28) Shin, H.; et al. Nonconventional Strain Engineering for Uniform Biaxial Tensile Strain in MoS_2 Thin Film Transistors. *ACS Nano* 2024, 18, 4414−4423.

(29) Zhang, Y.; Zhao, H. L.; Huang, S.; Hossain, M. A.; van der Zande, A. M. Enhancing Carrier Mobility in Monolayer MoS_2 Transistors with Process-Induced Strain. *ACS Nano* 2024, 18, 12377−12385.

(30) Jaikissoon, M. et al. CMOS-compatible Strain Engineering for High-Performance Monolayer Semiconductor Transistors. *arXiv Preprint*, arXiv:2405.09792, 2024. https://arxiv.org/abs/2405.09792.

(31) Azizimanesh, A.; Peña, T.; Sewaket, A.; Hou, W.; Wu, S. M. Uniaxial and biaxial strain engineering in 2D MoS_2 with lithographically patterned thin film stressors. *Appl. Phys. Lett.* 2021, 118, 213104.

(32) Pena, T.; Chowdhury, S. A; Azizimanesh, A.; Sewaket, A.; Askari, H.; Wu, S. M Strain engineering 2D MoS_2 with thin film stress capping layers. *2D Mater.* 2021, 8, 045001.

(33) Zhang, Y.; et al. Patternable Process-Induced Strain in 2D Monolayers and Heterobilayers. *ACS Nano* 2024, 18, 4205−4215.

(34) Shioya, H.; Russo, S.; Yamamoto, M.; Craciun, M. F.; Tarucha, S. Electron states of uniaxially strained graphene. *Nano Lett.* 2015, 15, 7943−7948.

(35) Jaikissoon, M.; Pop, E.; Saraswat, K. C. Strain Induced by Evaporated-Metal Contacts on Monolayer MoS_2 Transistors. *IEEE Electron Device Lett.* 2024, 45, 1528−1531.

(36) Nix, W. D. Mechanical properties of thin films. *Metall. Trans. A* 1989, 20, 2217−2245.

(37) Zhang, Z.; Hoang, L.; Hocking, M.; Peng, Z.; Hu, J.; Zaborski, G.; Dollard, P. D.; Goldhaber-Gordon, D.; Heinz, T. F.; Pop, E.; Mannix, A. J. Chemically Tailored Growth of 2D Semiconductors via Hybrid Metal-Organic Chemical Vapor Deposition. *ACS Nano* 2024, 18, 25414−25424.

(38) Wang, Y.; et al. Strain-induced direct−indirect bandgap transition and phonon modulation in monolayer WS_2. *Nano Res.* 2015, 8, 2562−2572.

(39) Michail, A.; et al. Tuning the Photoluminescence and Raman Response of Single-Layer WS_2 Crystals Using Biaxial Strain. *J. Phys. Chem. C* 2023, 127, 3506−3515.

(40) Li, Z.; Lv, Y.; Ren, L.; Li, J.; Kong, L.; Zeng, Y.; Tao, Q.; Wu, R.; Ma, H.; Zhao, B.; Wang, D.; Dang, W.; Chen, K.; Liao, L.; Duan, X.; Duan, X.; Liu, Y. Efficient strain modulation of 2D materials via polymer encapsulation. *Nat. Commun.* 2020, 11, 1151.

(41) Das, S.; et al. Transistors based on two-dimensional materials for future integrated circuits. *Nat. Electron.* 2021, 4, 786−799.

(42) Sebastian, A.; Pendurthi, R.; Choudhury, T. H.; Redwing, J. M.; Das, S. Benchmarking monolayer MoS_2 and WS_2 field-effect transistors. *Nat. Commun.* 2021, 12, 693.

(43) Amin, B.; Kaloni, T. P.; Schwingenschlögl, U. Strain engineering of WS_2, WSe_2, and WTe_2. *RSC Adv.* 2014, 4, 34561−34565.

(44) Khan, A. R.; Lu, T.; Ma, W.; Lu, Y.; Liu, Y. Tunable Optoelectronic Properties of WS_2 by Local Strain Engineering and Folding. *Adv. Electron. Mater.* 2020, 6, 1901381.

(45) Shen, T.; Penumatcha, A. V.; Appenzeller, J. Strain Engineering for Transition Metal Dichalcogenides Based Field Effect Transistors. *ACS Nano* 2016, 10, 4712−4718.

(46) Walter, T. N.; Cooley, K. A.; Domask, A. C.; Mohney, S. E. Nickel diffusion into MoS_2 and the effect of annealing on contact resistance. *Mater. Sci. Semicond. Process.* 2020, 107, 104850.

(47) Wang, X.; et al. Origins of Fermi Level Pinning for Ni and Ag Metal Contacts on Tungsten Dichalcogenides. *ACS Nano* 2023, 17, 20353−20365.

(48) Jaikissoon, M.; Ko, J. S.; Pop, E.; Saraswat, K. C. Local Back-Gate Monolayer MoS_2 Transistors with Channel Lengths Down to 50 nm and EOT ∼ 1 nm Showing Improved I_{on} using Post-Metal Anneal. In *2023 Device Research Conference (DRC)*, 2023; pp 1−2.

(49) Ortiz-Conde, A.; et al. A review of recent MOSFET threshold voltage extraction methods. *Microelectron. Reliab.* 2002, 42, 583−596.

Supporting Information

Understanding the Impact of Contact-Induced Strain on the Electrical Performance of Monolayer WS₂ Transistors

Lauren Hoang[1], Marc Jaikissoon[1], Çağıl Köroğlu[1], Zhepeng Zhang[2], Robert K. A. Bennett[1], Jung-Hwan Song[3], Jerry A. Yang[1], Jung-Soo Ko[1], Mark L. Brongersma[3], Krishna C. Saraswat[1,2], Eric Pop[1,2,4], and Andrew J. Mannix[2,5,*]

[1]*Department of Electrical Engineering, Stanford University, Stanford, CA 94305, USA*

[2]*Department of Materials Science & Engineering, Stanford University, Stanford, CA 94305, USA*

[3]*Geballe Laboratory for Advanced Materials, Stanford University, Stanford, CA 94305, USA*

[4]*Department of Applied Physics, Stanford University, Stanford, CA 94305, USA*

[5]*Stanford Institute for Materials and Energy Sciences, SLAC National Accelerator Laboratory, Menlo Park, CA 94025, USA*

1. Global Back-gated Device Fabrication and *n*-type Contact Resistance to WS₂

Monolayer WS₂ was grown by CVD directly onto 100 nm of SiO₂ with a Si (p^{++}) substrate serving as the global back-gate (**Figure S1a**). Discrete triangular monolayer WS₂ flakes were identified and used for the devices. XeF₂ was used to etch the WS₂ into well-defined channels, and transfer length method (TLM) structures with contact length L_C = 1.5 μm and varying channel lengths (L_{ch} = 100 nm–1 μm) were defined by electron beam (e-beam) lithography. We e-beam evaporate various contacts (Ni, Au, In, Sb) at ~10^{-8} Torr to examine the effects of metal contact on R_C. The exact metal splits used here were: Ni/Au (20/35 nm), Au (55 nm), In/Au (10/45 nm), Sb/Au (20/25 nm). Devices were measured in vacuum at 296 K before and after a 250 °C, 2 hour vacuum anneal. Annealing is commonly used to evaporate adsorbates off the TMD surface, resulting in lower hysteresis and improved current drive.
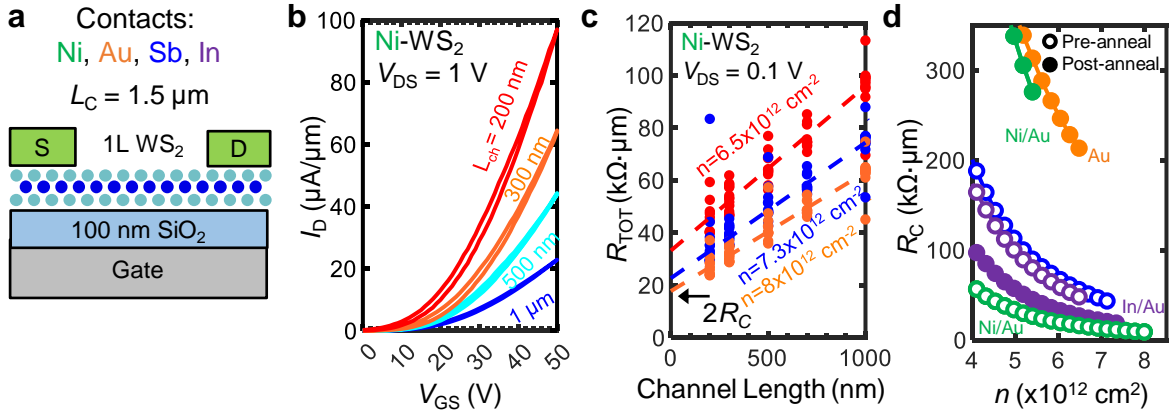

Figure S1. (a) WS₂ device schematic on 100 nm SiO₂. All devices were patterned with contact length L_C = 1.5 μm. **(b)** Current vs. gate voltage (V_{DS} = 1 V) of a L_{ch} = 1 μm, 500 nm, 300 nm and 200 nm channel for Ni contacts. **(c)** Total device resistance R_{TOT} vs. L_{ch} measured by TLM, at various carrier densities *n*, showing R_C extraction at the y-intercept. **(d)** Extracted R_C for various contact metals to WS₂, with Ni achieving the lowest contact resistance. Filled circles indicate data after 250°C annealing.

Figure S1b shows measured drain current (I_D) vs. gate voltage (V_{GS}) for Ni-contacted WS₂ with different channel lengths, before any annealing. The carrier density is obtained from the gate overdrive $V_{GS} - V_T$, where V_T was extracted by the constant-current method with a threshold current of $I_D = 10^{-2}$ μA/μm (IRDS high-performance limit). **Figure S1c** shows good linear fits to the total device resistance normalized by width (R_{TOT}) vs. L_{ch}. The vertical intercept of the linear fit yields the total contact resistance ($2R_C$). **Figure S1d** shows the R_C before and after annealing for all the contact metals (Ni, Au, Sb, In), with the lowest contact resistance obtained for Ni contacts pre-anneal. We uncover that the R_C significantly changes after annealing and is dependent on the contact metal. While Au has proven to be a good contact to MoS₂,[1] this was not the case for WS₂ and resulted in the highest R_C of the metals tested. Improvements in performance were seen when switching to Sb, In and Ni contacts. Sb contacts were not annealed due to thermal stability concerns.[2] While the In contacts improved with annealing, the Ni R_C worsened. Ni has been used as a standard contact for *n*-type WS₂ and is reaffirmed to be a good contact to WS₂, especially without any annealing.

2. Wafer-scale Ni/Au Stress Characterization

15/20 nm of Ni/Au was electron-beam evaporated at ~10^{-8} Torr onto a 350 μm thick (100) Si wafer terminated by native oxide. The wafer curvature was measured before metal deposition, after metal deposition, and after a 2 h, 150 °C vacuum anneal. Using the Stoney equation,[3] the film stress in the Ni/Au after e-beam deposition was found to be 160–175 MPa tensile. After the 150 °C 2 hour vacuum anneal, the film stress increased to 210–220 MPa tensile stress. Thin film force is given by $F = \sigma t$, where σ is the thin film stress and t is the thickness. The values found are summarized in **Table S1**. These values are consistent with the XRD data in **Supporting Information Section 10**, where the tensile in-plane strain increased with annealing.

Table S1: Extracted thin film stress from metal contact deposition.

Metal stack, nm	Anneal?	Stress σ, MPa	Thin film force, N/m
Ni/Au, 15/20	No	160–175	6
Ni/Au 15/20	Yes (150 °C, 2 hours)	210–220	7.5
Ni, 15	No	375– 410	6

3. Finite Element Analysis Simulations

Two-dimensional (2D) and three-dimensional (3D) stress simulations were performed for back-gated (BG) transistors, assuming linear elasticity. Multi-scale finite-element method simulations of the entire sample (including the transistor and the entire silicon substrate) confirmed that strains due to substrate bowing were negligible in comparison to those induced by the stressed contacts. To reduce simulation complexity, it thus suffices to simulate a smaller domain around the transistor with a fixed boundary condition at the bottom of a thinner section of substrate, with no appreciable errors in stress and strain distributions. In addition, we confirmed through 3D simulations that the WS_2 strain in the transistor width direction is small (WS_2 strain is essentially uniaxial and along the direction of current flow), as illustrated by **Figure S2**. Consequently, 2D simulations accurately capture the uniaxial stress and strain distributions in our devices, so the results presented in this work are generated using 2D simulations.
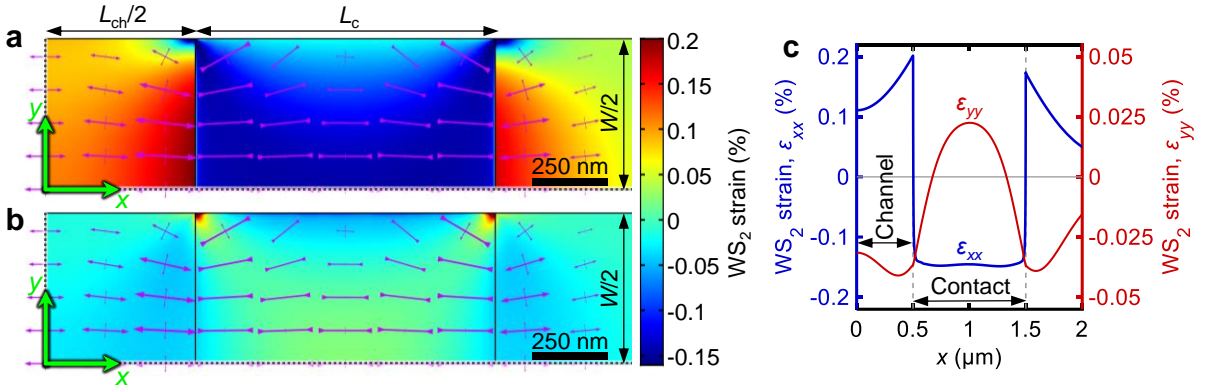

Figure S2. (a, b) The distributions of lengthwise in-plane strain [ε_{xx} given in (a)] and widthwise in-plane strain [ε_{yy} given in (b)] in WS_2 in a transistor with $L_{ch} = L_C = 1$ µm, viewed from above. The strain is induced by isotropic in-plane stress built into the contact electrodes. Only a quarter of the device is shown: the bottom left corner corresponds to the center of the device, with the dashed lines indicating the two symmetry planes. The magenta arrows indicate the principal strain directions at each point, showing that the strain is predominantly in the direction of current flow (i.e. along the x-axis) and hence approximately uniaxial, except very close to the edge of the channel. **(c)** WS_2 strains ε_{xx} (left axis) and ε_{yy} (right axis) along positive x-axis of the same device showing the widthwise strain is small (note the right axis is 4× smaller in scale).

In the finite element analysis, strain profiles are plotted against the x-coordinates of the unrelaxed geometry to consistently track and compare the same specific physical points across simulations. Each data point corresponds to a node, which retains its identity before and after relaxation. This method simplifies comparing strain profiles, as the x-coordinate always refers to the same physical point, despite deformation.

Since the stress in Au is small compared to Ni in the 15 nm Ni/20 nm Au stack, and given that Au is more mechanically compliant than Ni (i.e. lower in Young's modulus), we assume that the Au layer does not have a significant effect on the strain profile in WS_2 (at least before annealing) and is not included in the simulations. An in-plane tensile "initial stress" (the stress before the geometry is allowed to relax) of 400 MPa was assumed in Ni, equivalent to the 170 MPa of stress (6 N/m film force) of the thicker Ni/Au stack extracted from substrate bowing measurements. The isotropic elastic properties assumed for the materials other than WS_2 are summarized in **Table S2**. In contrast, WS_2 is only transversely isotropic (i.e. isotropic in-plane), and thus is described by an anisotropic stiffness tensor. Its elastic properties were taken from Li *et al.*,[4] and can be summarized as $E_{xx} = E_{yy} = 252$ GPa, $E_{zz} =$

50 GPa, $G_{xz} = G_{yz} = 26$ GPa, $v_{xy} = v_{yx} = 0.18$ and $v_{xz} = v_{yz} = 0.10$. Here, x and y correspond to the in-plane directions and z to the cross-plane direction, E denotes Young's modulus, G denotes shear modulus and v_{ij} denotes Poisson's ratio for loading along i and transverse direction j. The remaining elastic properties can be determined from these, e.g. $v_{zx} = (E_{zz}/E_{xx})v_{xz}$ and $G_{xy} = E_{xx}/[2(1 + v_{xy})]$. Any strain imparted on WS_2 during growth or transfer is not included in these simulations, so the simulated WS_2 strain results should be interpreted as relative to WS_2 as-transferred.

Table S2: Young's moduli and Poisson's ratios assumed for materials except for WS_2.

	Si	SiO$_2$	Pt	HfO$_2$[5,6]	Ni
Young's modulus (GPa)	170	70	400	170	70
Poisson's ratio	0.28	0.17	0.22	0.25	0.44

Due to poor adhesion provided by the weak van der Waals forces, it is possible for there to be some amount of relative displacement (and even slipping) between WS_2 and adjacent materials, especially between WS_2 and the underlying HfO_2.[7] A shear-lag model has previously been applied to 2D materials to capture this effect.[7–9] To implement it in simulations, we apply a boundary condition between WS_2 and HfO_2 that is equivalent to a very thin elastic adhesive, which acts as a bed of springs opposing the relative lateral displacement of WS_2 on HfO_2. The shear stiffness κ of the adhesive is equal to the lateral traction (force per unit area) per unit displacement, and quantifies how much lateral force it takes for WS_2 to slide on HfO_2. If κ is low enough such that WS_2 is sufficiently decoupled from the layer underneath, we may express the characteristic strain decay length[7,10] (also known as the shear-lag length) as $\lambda \cong (E't/\kappa)^{1/2}$, where t is the WS_2 thickness, $E' = E/(1 - v^2)$ is the effective in-plane Young's modulus of WS_2 constrained such that there is no strain along its width (also known as 2D P-wave modulus), and E and v are WS_2's in-plane Young's modulus and Poisson's ratio, respectively.
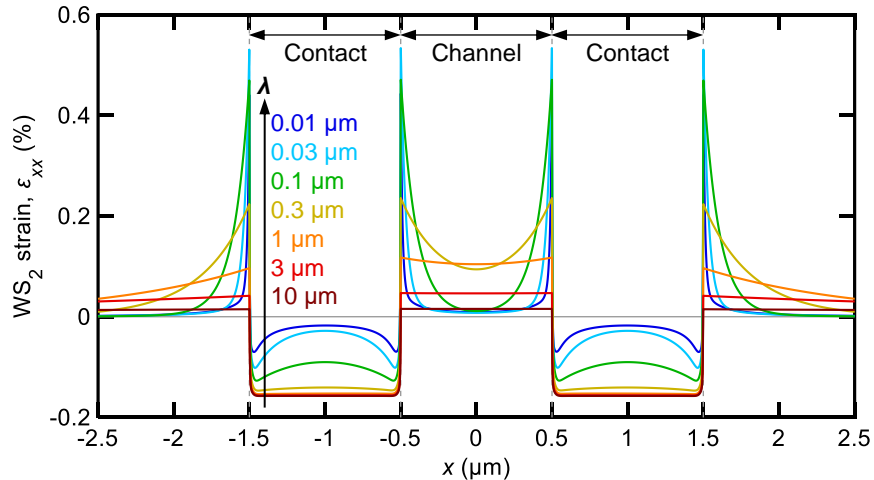

Figure S3. The contact-induced in-plane strain distribution in WS_2 in a transistor with $L_{ch} = L_C = 1$ μm, for several different values of characteristic strain decay length λ, which is approximately inversely proportional to the square root of the restoring shear "spring constant" which couples WS_2 to the underlying HfO_2. Weaker coupling (easier sliding) generally yields a lower peak strain and a more uniform strain distribution in the channel. $\lambda = 0.5$ μm is assumed in the other simulation results presented in this work.

Values of λ ranging from about 0.3 µm to 15 µm have been reported for various monolayer 2D materials on bulk substrates.[7,9,11–14] For our WS_2 films on SiO_2, photoluminescence measurement results in **Figure 2c-d** suggest that λ is comparable to 0.5 µm, so we have chosen $\lambda = 0.5$ µm (corresponding to $\kappa = 650$ MPa/µm) for our simulations of WS_2 on HfO_2 as a reasonable estimate. This value is also close to what has been reported for WS_2 on a polymer substrate.[12] The impact of other possible values of κ (and hence λ) on the strain profile in a transistor with $L_{ch} = L_C = 1$ µm is explored in **Figure S3.** It can be seen that for very high κ (no slip), only the region of the channel within ~50 nm of the contacts have appreciable strain. Much more of the channel is strained if WS_2 is able to slide more easily on HfO_2, and the entire channel is strained if λ is comparable to or greater than L_{ch}. For very small κ ($\lambda \gg L_{ch}$), the compressive strain under the contract is balanced by a small strain distributed mostly in a long region beyond the contacts ($x > 1.5$ µm in **Figure S3**), so the channel strain is likewise small.
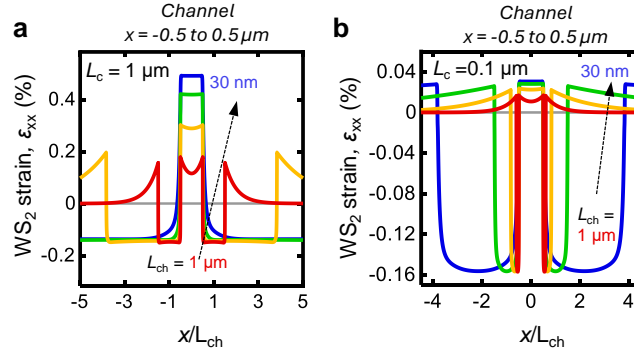

Figure S4. (a) Simulated horizontal strain profile along a device with $L_C = 1$ µm and $L_{ch} = 1$ µm, 300 nm, 100 nm, and 30 nm. The x position is normalized by L_{ch}, for easier visualization of different channel lengths. **(b)** Simulated horizontal strain profile along a device with $L_C = 0.1$ µm and $L_{ch} = 1$ µm, 300 nm, 100 nm, and 30 nm. Similar to panel a), the x position is normalized by L_{ch}.

Figure S4a,b demonstrates the compressive strain under the contacts, which appears to be relatively similar in magnitude, regardless of channel length. At the beginning of the contact ($x = 0$), the WS_2 strain appears to abruptly switch from tensile to compressive (**Figure S5a,b**). Under the contacts, the WS_2 is most compressive at the center of the contact, reaching a maximum of -0.15% compressive strain (**Figure S5a,b**). Outside the contact edges, the WS_2 strain is tensile then decays to "unstrained/neutral" away rom the contact edge.
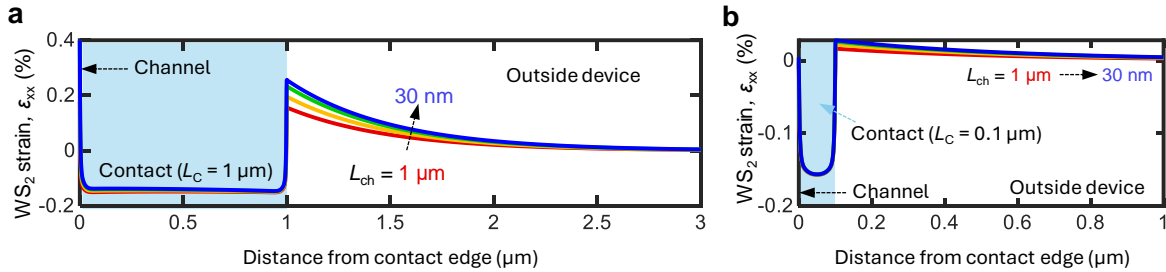

Figure S5. (a) Simulated horizontal strain profile along a device with $L_C = 1$ µm and $L_{ch} = 1$ µm, 300 nm, 100 nm, and 30 nm. The position x is normalized by L_{ch}, for easier visualization of different channel lengths. **(b)** Simulated horizontal strain profile along a device with $L_C = 0.1$ µm and $L_{ch} = 1$ µm, 300 nm, 100 nm, and 30 nm. **(c)** Simulated horizontal strain profile of WS_2 along a device with $L_C = 1$ µm and $L_{ch} = 1$ µm, 300 nm, 100 nm, and 30 nm from the inner contact edge at $x = 0$. **(d)** Simulated horizontal strain profile of WS_2 along a device with $L_C = 0.1$ µm and $L_{ch} = 1$ µm, 300 nm, 100 nm, and 30 nm from the inner contact edge at $x = 0$.

4. Photoluminescence Spectroscopy on WS$_2$

Monolayer WS$_2$ grown on sapphire was transferred onto thermally oxidized 100 nm SiO$_2$/Si and then patterned using electron-beam lithography. Ni/Au 15/20 nm was electron-beam evaporated for the contact features (as described in the Methods section). Spatially-resolved photoluminescence measurements of the WS$_2$ monolayer devices were obtained by confocal spectroscopy (Witec confocal Raman imaging microscope). To obtain the spatial map, the sample was exposed to a tightly focused 532 nm laser spot ($\times$50 objective, NA = 0.55) using a high-resolution closed loop XYZ piezo scan stage. The excitation laser power was set to 126 μW and the photoluminescence signal was collected by the same objective lens and filtered by a dichroic filter cube and a long wave pass edge filter (Semrock, LP03-532RU-25).

To track the photoluminescence (PL) peaks, we fit the PL mapping spectra using an iterative least-square method in MATLAB. All PL spectra were taken from 1.78 eV to 2.2 eV and the baseline of the spectra were subtracted prior to fitting. Two peaks were used to fit the PL spectrum using a weighted Gaussian-Lorentzian line shape for all the peaks (**Figure S6a**). The higher energy (A exciton) peak was plotted for **Figure 2d,f** instead of the A$^-$ lower energy shoulder peak. Both peaks were confirmed to show the same redshift with strain away from the contact, as well as the peak position for the combined PL peak (**Figure S6b**).
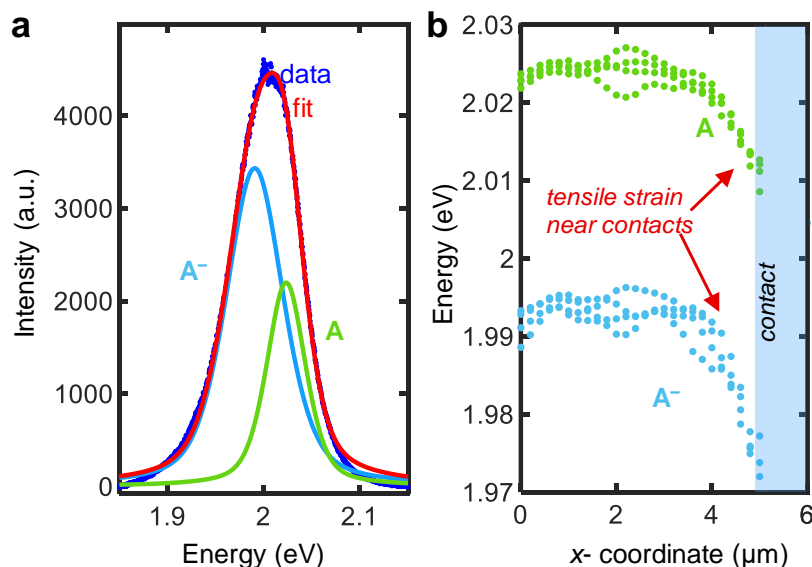

Figure S6. Photoluminescence measurements of WS$_2$ for strain determination. **(a)** PL spectra and peak fitting of A and A$^-$ peaks. **(b)** Extracted WS$_2$ PL peak position of A and A$^-$ peak position as a function of x-coordinate away from the contact edge (on the right). Plot uses data from **Figure 2d** and shows that both A and A$^-$ peaks are redshifted near the contact, corresponding to tensile strain near the contact.

5. Literature Comparison for R_C in WS₂ and Annealing Conditions

Table S3: Benchmarking the electrical performance of WS₂ transistors.

Ref	WS₂ layers	Contact Metal	Annealed Contacts?	L_C (nm)	I_{on} (µA/µm)	L_{ch} (nm)	R_C (kΩ·µm)
This Work	**1L**	**Ni/Au (15/20 nm)**	**No**	**1 µm**	**223**	**50**	**1.73**
This Work	**1L**	**Ni/Au (15/20 nm)**	**No**	**0.1 µm**	**80**	**50**	**7.7**
15	1L	Au	No	Not reported	10	600	-
16	2L	Ni/Pd	Yes-250 °C	Not reported	310	100	1.6
17	2L	Ni/Pd	Yes-250 °C	Not reported	210	100	2.38
18	3-7L	Ni	385 K 6 h vacuum	Not reported	600	40	0.5
19	1L	Bi (20 nm)	No	Not reported	46	320	1.3
20	1L	Sb/Au (20/20)	No	~ 1 µm from SEM	243	135	0.73
20	1L	Bi/Au (20/20)	No	~ 1 µm from SEM	250	135	0.63
21	1L	Bi/Au (20/15 nm)	No	Not reported	400	100	-
22	1L	Ni/Au (20/40 nm)	No	~ 1 µm from SEM	325	50	1.1 (BeO)
22	1L	Ni/Au (20/40 nm)	No	~1 µm from SEM	170	50	2.6 (HfO₂)
23	1L	Ni (50 nm)	No	Not reported	150	290	1.2
24	2L	Ni/Au (20/40nm)	No	Not reported	635	18	0.38
24	1L	Ni/Au (20/40nm)	No	Not reported	267	80	0.72
25	2L (3R)	Ni/Au (20/60nm)	No	1 µm	480	50	0.67
26	1L	Ni/Au (40/30nm)	No	~ 1-1.3 µm from SEM	26	100	2.1
27	1L	Ni/Au (40/30nm)	No	Not reported	20	100	-

6. Transfer Length Determination for Ni Contacts on WS$_2$

The transfer length is given by $L_T = (\rho_C/R_{sh}')^{1/2}$, where R_{sh}' is the sheet resistance of the 2D channel under the contacts in $\Omega/\square$, and ρ_C is the specific contact resistivity given in $\Omega \cdot \mu m^2$. Contact resistance is can be expressed as $R_C = (\rho_C R_{sh}')^{1/2} \coth(L_C/L_T)$.

In the case when $L_C > 1.5\,L_T$ like in our $L_C = 1\,\mu m$ case, $R_C = (\rho_C R_{sh}')^{1/2} \coth(L_C/L_T) \approx (\rho_C R_{sh}')^{1/2}$. If we assume that $R_{sh}' = R_{sh}$ (the sheet resistance of WS$_2$ in the channel is the same as the resistance underneath the contacts), we can estimate the L_T of our Ni–WS$_2$ devices. For the $L_C = 1\,\mu m$ devices, fitting the median TLM devices at an overdrive voltage of $V_{ov} = 1.95$ V yields a $R_C = 2.49\,k\Omega \cdot \mu m$ and $R_{sh} = 45\,k\Omega$ (**Figure S7a**). This would yield $L_T = 63.5$ nm, which is comparable to other results in 2D literature, in the 7–45 nm range.[28,29] When using the R_C extracted from the *best* TLM (1.7 k$\Omega \cdot \mu m$), the extracted L_T is 37 nm. Additionally, this extracted L_T could be considered the upper bound of the transfer length, since the R_{sh}' under the contacts would likely undergo contact deposition-induced damage, which could thus increase R_{sh}' and lower L_T. With $L_T = 37$ nm (63.5 nm), a $L_C = 100$ nm contact would increase in R_C due to current crowding at a maximum of 0.9% (8.9%). Thus, current crowding cannot solely explain the $> 5\times$ increase in contact resistance seen when $L_C = 100$ nm.

We also fabricate additional devices with $L_C = 200$ nm to confirm that our measured 100 nm devices are greater than the transfer length. We see that the $L_C = 1\,\mu m$ still shows significant improvement in on-state current than the $L_C = 200$ nm devices (**Figure S7b**).
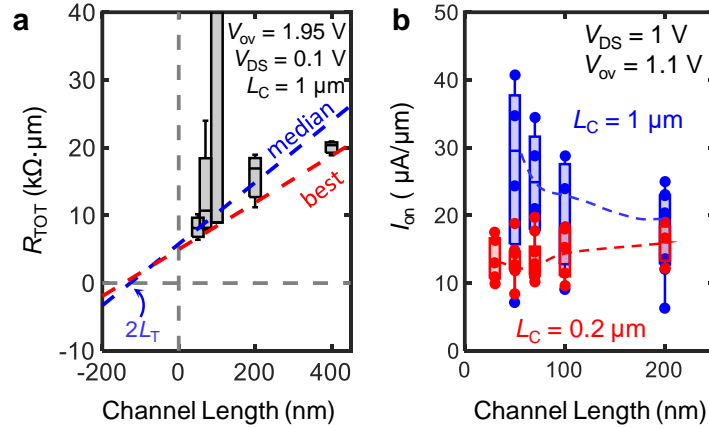

Figure S7. (a) Total device resistance R_{TOT} vs. channel length L_{ch}, at a fixed overdrive voltage $V_{ov} = 1.1$ V for a $L_C = 1\,\mu m$ device, showing linear fit of best devices (red) as well as median devices (blue). **(b)** On-state current (I_{on}) at a fixed overdrive $V_{ov} = 1.1$ V versus L_{ch}, comparing $L_C = 1\,\mu m$ and $L_C = 0.2\,\mu m$, devices.

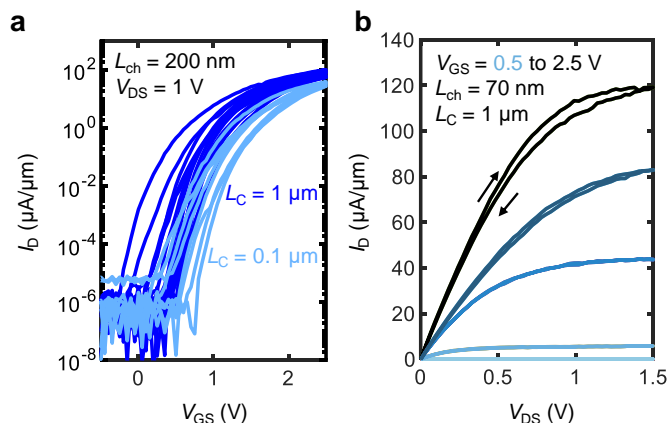## 7. Additional Electrical Characterization and Analysis of Ni–WS₂ Devices on HfO₂

Figure S8. (a) Measured I_D vs. V_{GS} curves in log scale for all L_{ch} = 200 nm devices with L_C = 1 μm (8 devices) and L_C = 0.1 μm (4 devices). Forward and backward sweeps are plotted with clockwise hysteresis. **(b)** Measured I_D vs. V_{DS} curve for a representative L_{ch} = 70 nm device. Note the proper current saturation at relatively low voltage, due to the small, positive V_T.
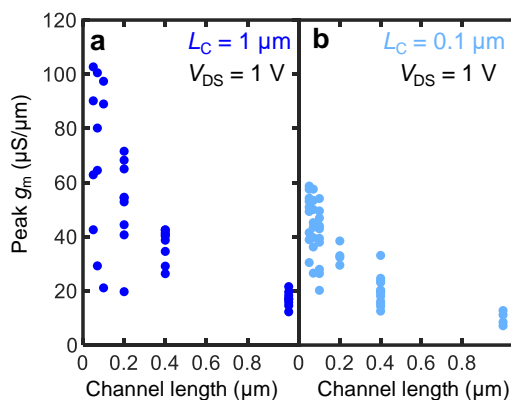

Figure S9. (a) Peak transconductance (g_m) vs. channel length for L_C = 1 μm. **(b)** Peak g_m vs. channel length for L_C = 0.1 μm.

Figure S10a compares the threshold voltage for long and short contacts, where most devices have a small, and positive V_T. For every channel length, the median V_T for long contact devices is more negative (**Figure S10a**). The boxplot in **Figure S10b** demonstrates that the long contact device has a median V_T = 0.56 V, compared to the short contact devices at V_T = 0.83 V. **Figure S10c** shows the hysteresis of the HfO₂ devices with various contact lengths plotted versus channel length. This was extracted at $I_D = 10^{-2}$ μA/μm.

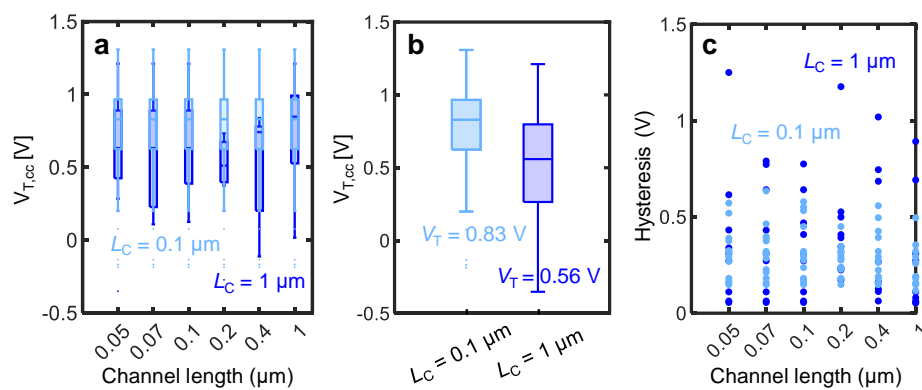**Figure S10.** (a) Threshold voltage (V_T) extracted at $I_D = 10^{-2}$ µA/µm vs. channel length, for both long and short contact devices. (b) Boxplot of V_T for short and long contact devices, showing a more negative V_T for long contact devices. (c) Hysteresis at $I_D = 10^{-2}$ µA/µm with respect to channel length, for both long and short contacts, showing a much larger spread, and larger hysteresis for long contact devices.

8. Schottky Barrier Height Extraction

Additional devices were fabricated to confirm reproducibility of the strain effect of Ni contacts and to determine the Schottky barrier height (**Figure S11a**). Monolayer WS_2 was grown by CVD and then wet transferred onto 100 nm SiO_2 with pre-patterned alignment marks. The transfer process is described in the Methods Section. Coarse pads and channel definition were patterned and etched with XeF_2 into TLM structures with $L_C = 1$ μm and $L_C = 0.1$ μm. The fine contact step was patterned, then 15/20 nm Ni/Au were electron-beam deposited at ~ 10^{-8} Torr. The $L_C = 1$ μm devices showed roughly an order of magnitude increase in I_D at $V_{GS} = 50$ V, compared to the $L_C = 0.1$ μm devices (**Figure S11b**), as well as a negative threshold voltage shift for the long contact devices. This confirms the repeatability and generalization of our findings.
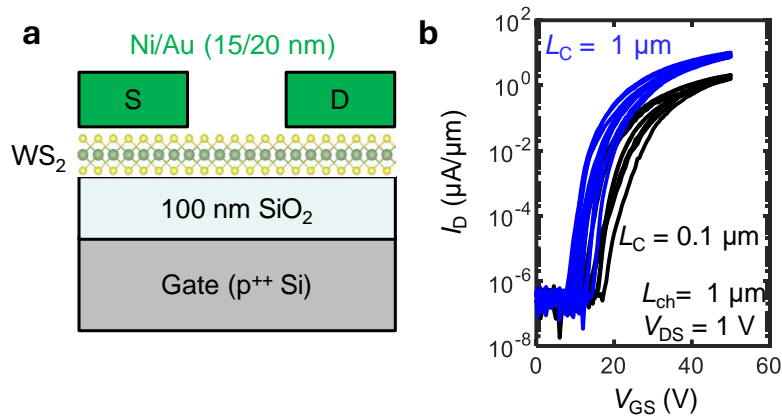

Figure S11. (a) Cross-section schematic of monolayer WS_2 transferred from sapphire onto 100 nm SiO_2 with electron-beam evaporated Ni/Au contacts. **(b)** Measured I_D vs. V_{GS} curves for $L_{ch} = 1$ μm devices with $L_C = 1$ μm (blue) and $L_C = 0.1$ μm (black), showing clear I_D improvement with long contacts. Both forward and backward sweeps are plotted, showing clockwise hysteresis.

For Schottky barrier height extraction, temperature-dependent measurements were conducted on 3 devices with $L_C = 1$ μm and 3 devices with $L_C = 0.1$ μm, all with $L_{ch} = 1$ μm. We estimate the Schottky barrier height (SBH, ϕ_B) from a procedure previously documented.[30] The thermionic emission current is given by $I_D = A_{2D}^* T^{\frac{3}{2}} \exp\left(-\frac{q\phi_B}{k_B T}\right)\left[1 - \exp\left(-\frac{qV}{k_B T}\right)\right]$, where A_{2D}^* is the 2D-equivalent Richardson constant, T is the temperature, k_B is Boltzmann's constant, q is the elementary charge, and V is the applied voltage. **Figure S12a,d** displays the transfer curves (I_D-V_{GS}) at each temperature, ranging from 193 K–313 K in steps of 20 K, for a $L_C = 0.1$ μm and $L_C = 1$ μm device. From the I_D-V_{GS} curves, an Arrhenius plot of $\ln(I_D/T^{\frac{3}{2}})$ vs $1000/T$ can be plotted for each voltage (V_{GS}) (**Figure S12b,e**), where the slope is the barrier height ϕ_B at that particular V_{GS}. The extracted barrier height is then plotted in **Figure S12c,f** for short and long contacts, respectively. The effective barrier height at the flat band voltage is estimated by the point at which the barrier height deviates from the linear fit (as seen in **Figure S12c,f**). For devices with $L_C = 0.1$ μm, barrier heights of 0.34 eV, 0.40 eV and 0.40 eV were extracted. For devices with $L_C = 1$ μm, barrier heights of 0.17 eV, 0.20 eV and 0.25 eV were extracted. On average, this corresponds to a barrier height lowering of 0.17 eV when switching to long contacts.
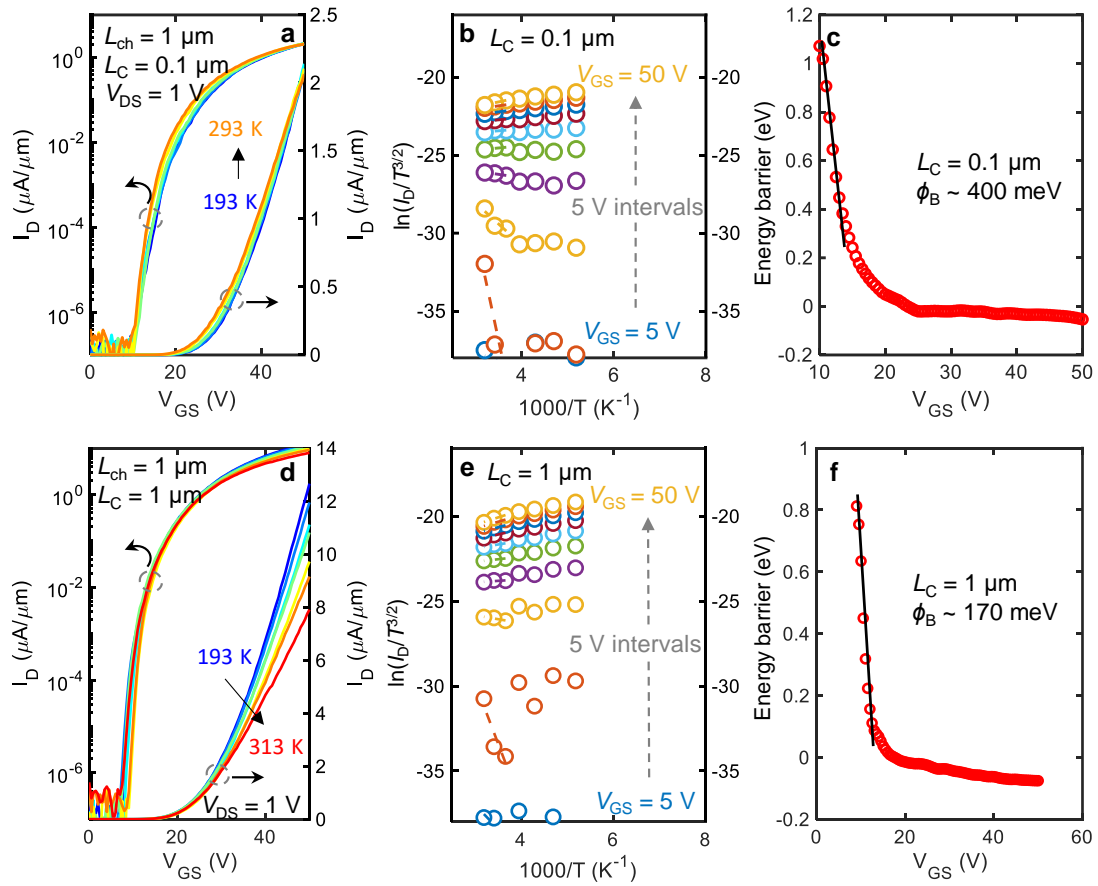
Figure S12. Schottky barrier height extraction of a typical L_{ch} = 1 μm Ni-WS$_2$ FETs on 100 nm SiO$_2$. **(a-c)** L_C = 0.1 μm and **(d-f)** L_C = 1 μm. **(a), (d)** Temperature-dependent I_D–V_{GS} measured at V_{DS} = 1 V. **(b), (e)** Arrhenius plots of Ni–WS$_2$ FETs for V_{GS} from 5 V to 50 V. **(c), (f)** Extracted electron Schottky barrier height.

9. Utilizing Capping Layers for Thermal Processing

Capping layers can be used to pin the WS_2 channel during thermal annealing, in order to maintain the strain profile in a device. Here, 1.5 nm Al was electron-beam evaporated on the HfO_2 local back-gate devices. Then, 10 nm AlO_x was deposited by thermal atomic layer deposition at 130°C (**Figure S13a**). The devices were measured before capping, after capping, and after a 150°C 2 hour vacuum anneal. The long contacts devices did not show any degradation in performance, even showing an increase in I_D (**Figure S13b**). In capped devices, the WS_2 is less likely to slip from the substrate. The top oxide layer can "pin down" the WS_2 in place. This contrasts the uncapped devices, which showed lower I_D after annealing (**Figure 4a,c**). The short contact devices did not show a significant change in performance after annealing **(Figure S13c)**. Future work is needed to determine how the strain profile is influenced by encapsulation, thermal processing, and different device geometries (e.g. gate-all-around, dual-gate structures), for industry relevant processing.
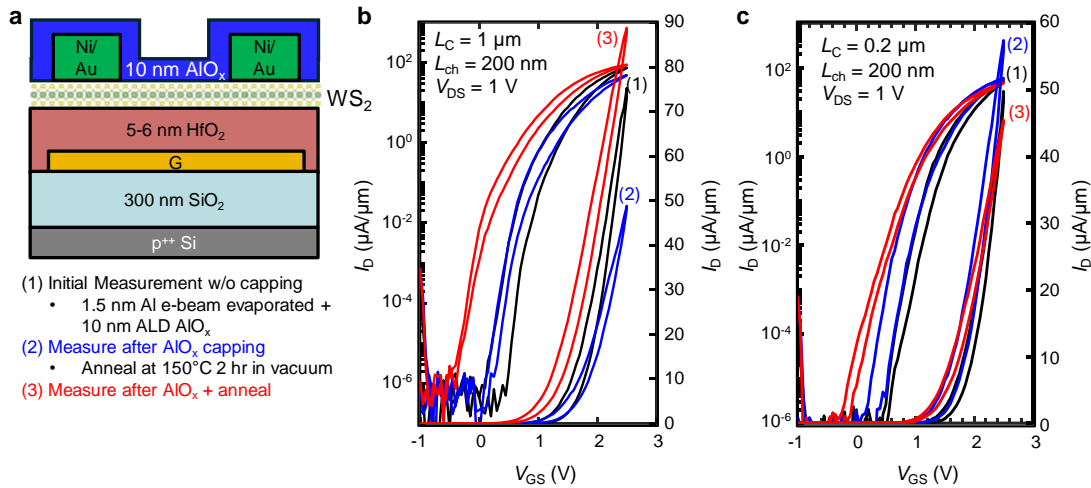

Figure S13. **(a)** Device schematic of a local back-gated monolayer WS_2 transistor after AlO_x capping (top) and device fabrication process with device measurement steps after device fabrication (bottom). Stages (1) - (3) are denoted for panels (b,c) **(b)** Measured I_D vs. V_{GS} for a L_C = 1 µm device with L_{ch} = 200 nm. The 3 stages of the single device are plotted (as given by panel (a), bottom). **(c)** Measured I_D vs. V_{GS} for a L_C = 0.2 µm device with L_{ch} = 200 nm. All measurements are taken at room temperature at ~10^{-4} Torr vacuum probe station.

10. Strain Evaluation of Contact Metal Thin Films via X-ray Diffraction

We quantified changes in the structure and stress state of the Ni/Au films using in-plane X-ray diffraction. Continuous monolayer WS_2 was transferred from sapphire onto SiO_2/Si. To mimic the make-up of our WS_2 contacts, 15/20 nm Ni/Au was then blanket-deposited on top. X-ray diffraction measurements were conducted using a PANalytic Empyrean system with a Cu-Kα target. All in-plane measurements were conducted with χ (as defined previously[31]) at 88.5°– 89.25° to measure the in-plane diffraction peaks at various diffraction angles (2θ). To measure the changes in the Ni in-plane strain, only 15 nm of Ni was deposited: due to the shallow angle of the X-ray beam, the X-rays were all absorbed in the top Au layer. Symmetric $\theta/2\theta$ scans were used to verify the planes present in the films. We separately measured the changes in Ni strain on fused silica (amorphous SiO_2) to confirm that the nearby crystalline Si diffraction peaks were not convolved in our measurement.
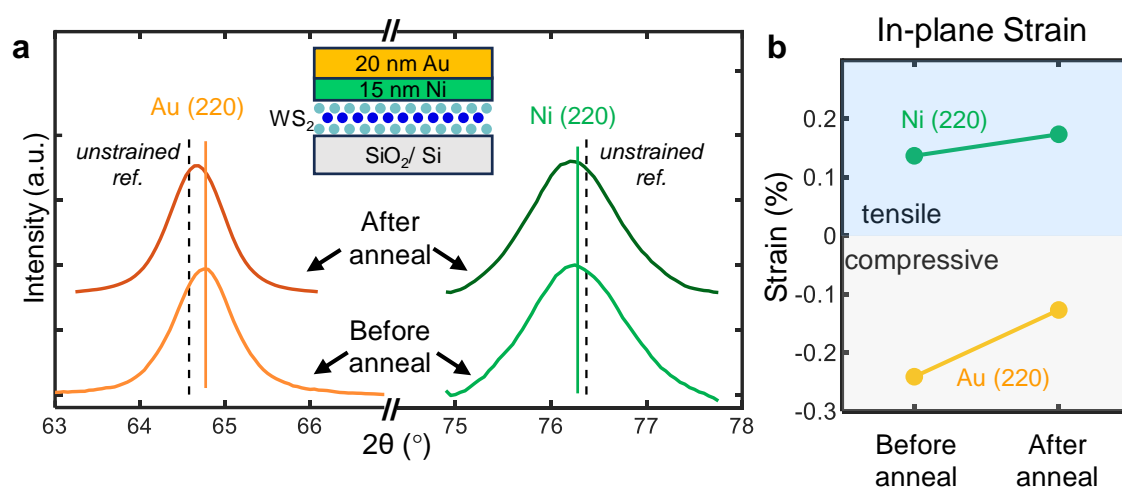

Figure S14. X-ray diffraction for in-plane strain in metal films. **(a)** In-plane XRD spectra of the Au (220) and Ni (220) peaks collected before and after annealing at 150 °C. **(b)** Calculated in-plane strain in the Ni and Au layers before and after annealing.

Ni was found to evaporate with a high degree of in-plane tensile strain (0.137%), while Au is evaporated with some compressive strain (**Figure S14a,b**). The high degree of tensile in-plane strain in the Ni combined with its high Young's modulus (~200 GPa) is responsible for the substantial strain induced in the WS_2 contact region, which is much more mechanically compliant than the Au film.

After annealing, we observe that the in-plane strain of both contact metals becomes more tensile, from 0.137% to 0.174% for Ni and from -0.241% to -0.127% for Au (**Figure S14a,b**). Annealing is seen to more dramatically affect the Au layer, which becomes much more tensile in-plane. This is expected as Au has a higher thermal expansion coefficient than Ni. There may also be additional transient strains due to differences in thermal expansion coefficients that impact the strain in Ni, Au, and WS_2. One could manipulate the thermal response by carefully considering a metal's oxidation potential and its thermal response, as well as the impacts of a bilayer metal stack. One way to overcome the effect of annealing is to potentially use a low expansion contact such as iron-nickel alloys.[32]

From initial in-plane measurements on the SiO_2/Si substrate, the Ni (220) peak was determined to be in-plane oriented. However, the Ni (220) closely aligns to the Si (331) peak. To reaffirm that the peaks measured were from Ni, continuous monolayer WS_2 was also transferred onto fused silica. Again, 15 nm Ni was blanket deposited onto the continuous monolayer WS_2 by electron beam evaporation. **Figure S15** validates that 1) the in-plane peak is once again Ni (220), and that 2) the peak positions and thus strain of the Ni film deposited on both fused silica and SiO_2/Si are the same.
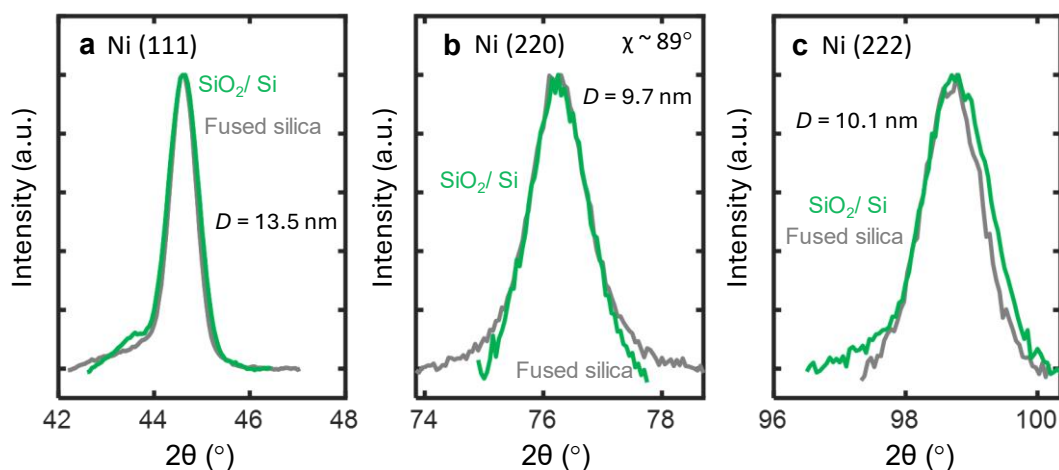

Figure S15. X-ray diffraction on Ni film blanket deposited on SiO_2/Si (green) and fused silica (grey). **(a)** Ni (111) peak. **(b)** Ni (220) peak. **(c)** Ni (222) peak. D is the average grain size, calculated from the Scherrer equation.

We note that decoupling grain size from stress effects is difficult. For polycrystalline metal films that grow in the Volmer-Weber mode (like Ni), it is understood that stresses developed during deposition are related to the morphologies and microstructures of the growing films. The development of a tensile coalescence stress is understood to be from grain boundary formation and thus grain size and stress are linked.[33]

Evaporated Ni metal grains are typically on the order of a few nanometers (<5 nm) initially, which increases to 20 nm in a 70 nm-thick Ni film.[34] Using the Scherrer equation for the XRD spectra in **Figure S15**, the average grain size is 13.53 nm, 9.70 nm, 10.10 nm, for the spectra obtained for the Ni (111), (220), and (222) on fused silica, respectively. This is an order of magnitude lower than the shortest contact length (100 nm) used. Thus, we don't expect the grain size to vary significantly between the two contact lengths.

11. Effect of Annealing on Ni–WS₂ Devices on SiO₂

Ni-contacted monolayer WS₂ devices were fabricated on 100 nm SiO₂ as described in **Supporting Information Section 1** and **Figure S1**, on top of WS₂ directly grown on the SiO₂. 20/35 nm Ni/Au was used as the contacts, with device width $W = 2$ μm and $L_C = 1.5$ μm. **Figure S16** displays the transfer curves of the devices for $L_{ch} = 100$ nm–1 μm. Initially, there was low yield of the $L_{ch} = 100$ nm devices, probably due to the stress imparted by the contact stack for short channel dimensions, causing cracking. After a 250°C 2 hour vacuum anneal, the same trend was seen as the 150°C anneal for long contact devices, where the I_{on} and R_C worsened with annealing.
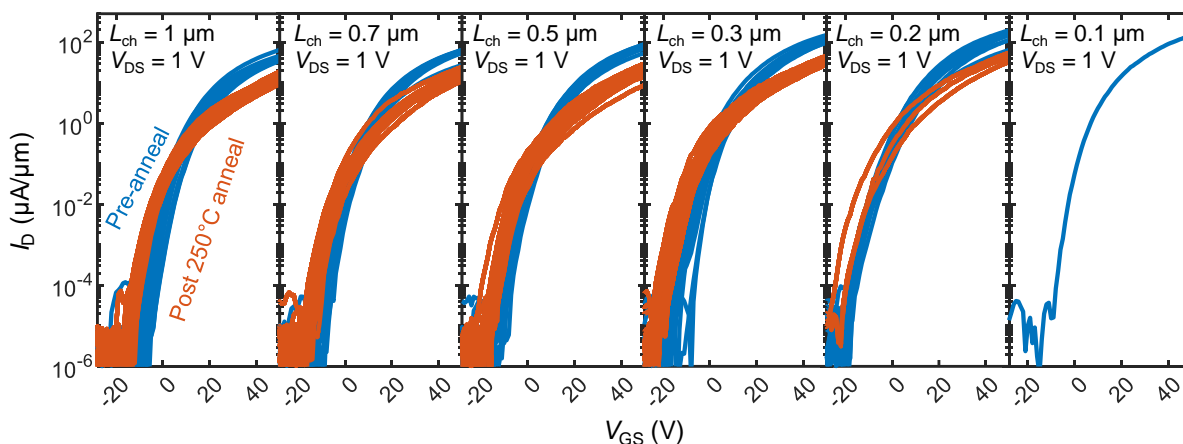

Figure S16. Transfer curves of working devices for Ni contacts on monolayer WS₂ with a 100 nm SiO₂ gate dielectric ($L_{ch} = 100$ nm–1 μm, $W = 2$ μm and $L_C = 1.5$ um), for before and after vacuum annealing at 250°C. Only forward sweep has been plotted for clarity.

After the 250 °C anneal, very few of the $L_{ch} = 200$ nm devices worked, and the majority of the devices were open circuit when measured. In comparison, all the long channel devices ($L_{ch} = 0.7$-1 μm) that worked pre-anneal, worked after annealing (**Figure S17a**). The devices were examined using scanning electron microscopy (SEM) to find the root cause of failure. For the 200 nm and 300 nm devices that worked before annealing but not after annealing, a crack across the channel was seen in the WS₂ (**Figure S17b**). The evidence of cracking as well as the likelihood to affect shorter channels, illustrates the high stress in the WS₂ especially for the short channel devices. Additionally, the cracking arising specifically from annealing demonstrates the high stress WS₂ experiences during annealing with Ni/Au contacts. This is supported by the XRD results in **Supporting Information Section 10** that indicates increased tensile strain in both the Ni and Au with annealing.
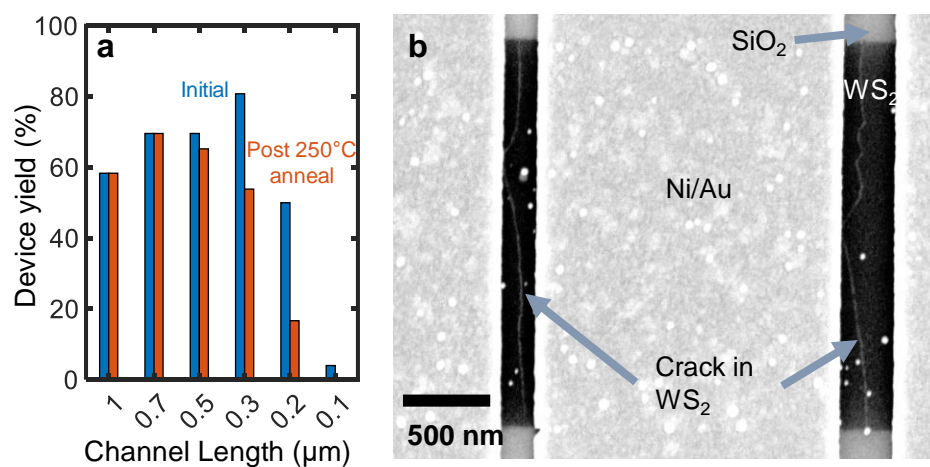
Figure S17. (a) The number of working devices at each channel length, before and after annealing, for devices shown in **Figure S16. (b)** Scanning electron microscopy (SEM) image of a Ni/Au 20/35 nm device, showing cracking in both the $L_{ch} = 200$ nm (left) and $L_{ch} = 300$ nm (right) after undergoing a 250 °C vacuum anneal.

12. Density Functional Theory Simulations

Density functional theory (DFT) simulations were performed using Quantum ESPRESSO version 7.1.[35] We use spin-orbit coupling and fully relativistic norm-conserving Vanderbilt pseudopotentials.[36,37] The energy band diagrams were extracted as functions of biaxial and uniaxial strain, similar to our previous work,[38] and corresponding band gaps were determined (**Figure S18a**). Biaxial and uniaxial tensile strain both lead to a band gap reduction, mainly through the lowering of the conduction band edge at the K point. Here, we extract both the movement of the conduction band edge and valence band edge with respect to strain, showing that tensile strain highly impacts the movement of the conduction band edge at a much faster rate than the valence band edge (**Figure S18b**). DFT calculations suggest that an average reduction of 170 meV in conduction band minimum (i.e., barrier height, **Figure 3f),** corresponds to ~1.5% uniaxial strain induced in the WS_2 near the contacts. This is in reasonable agreement with the values obtained from finite-element analysis simulations (~0.2–0.6%) and photoluminescence (~0.7%) (**Figure 2f**).
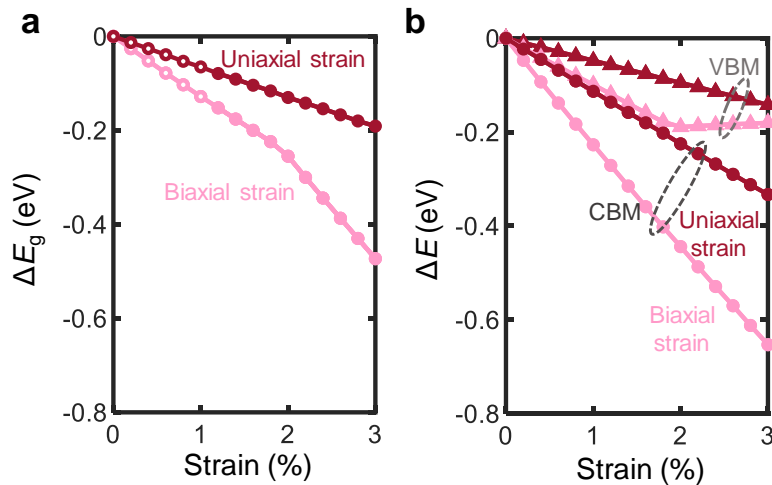

Figure S18. (a) Calculated energy band gap reduction (ΔE_g) for uniaxial and biaxial tensile strain. Hollow circles denote data from Yang et al.[33] **(b)** Change in energy of conduction band minimum (CBM) and valence band maximum (VBM) under uniaxial tensile strain (dark red) and biaxial tensile strain (pink).

13. Finite Element Analysis Simulations with Varying Ni Thickness

The strain profile of WS$_2$ was also simulated with different Ni contact thicknesses (**Figure S19**) of 5 nm and 50 nm (in addition to the 15 nm in all other simulations), with a fixed film stress of 400 MPa. The strain in the TMD has been shown to be proportional to the thin film force.[7,39,40] **Figure S20** shows that as the Ni thickness (and thus film force) increases, the tensile strain in the WS$_2$ channel increases.
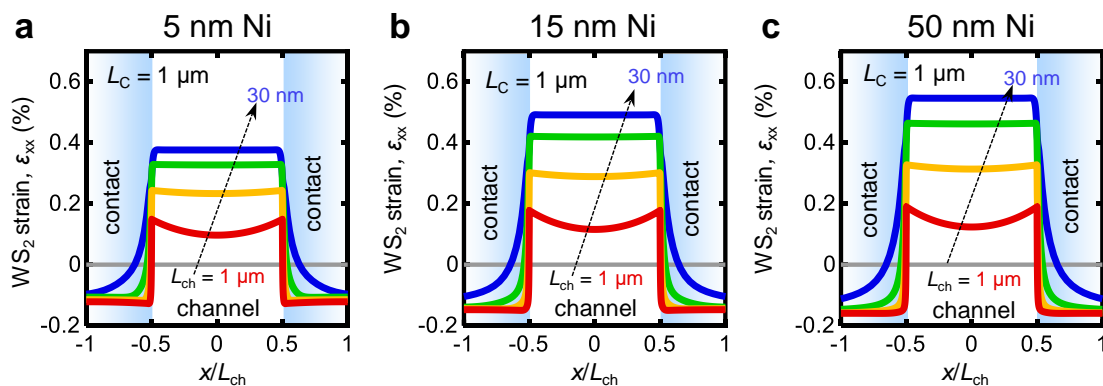

Figure S19. Simulated horizontal strain profile along a device with L_C = 1 μm and L_{ch} = 1 μm, 300 nm, 100 nm, and 30 nm with Ni contact thickness of **(a)** 5 nm **(b)** 15 nm **(c)** 50 nm. The position x is normalized by L_{ch}, for easier visualization of different channel lengths.

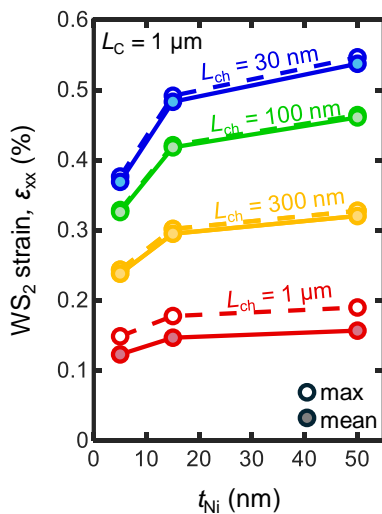**Figure S20**: Simulated horizontal strain of WS$_2$ as a function of Ni contact thickness for L_C = 1 μm and L_{ch} = 1 μm, 300 nm, 100 nm, and 30 nm. Filled circles denote the mean strain, open circles denote the maximum strain value in the channel.

REFERENCFES FOR SI

1. English, C. D., Shine, G., Dorgan, V. E., Saraswat, K. C. & Pop, E. Improved Contacts to MoS$_2$ Transistors by Ultra-High Vacuum Metal Deposition. *Nano Lett.* **16**, 3824–3830 (2016).
2. Chou, A.-S. *et al.* Antimony Semimetal Contact with Enhanced Thermal Stability for High Performance 2D Electronics. in *2021 IEEE International Electron Devices Meeting (IEDM)* 7.2.1-7.2.4 (IEEE, 2021). doi:10.1109/IEDM19574.2021.9720608.
3. Janssen, G. C. A. M., Abdalla, M. M., van Keulen, F., Pujada, B. R. & van Venrooy, B. Celebrating the 100th anniversary of the Stoney equation for film stress: Developments from polycrystalline steel strips to single crystal silicon wafers. *Thin Solid Films* **517**, 1858–1867 (2009).
4. Li, L., Zeng, Z. Y., Liang, T., Tang, M. & Cheng, Y. Elastic properties and electronic structure of WS$_2$ under pressure from first-principles calculations. *Z. Naturforsch. A* **72**, 295–301 (2017).
5. Vargas, A. L. M., De Araújo Ribeiro, F. & Hübler, R. Changes in the Young Modulus of hafnium oxide thin films. *Nucl. Instrum. Methods Phys. Res., Sect. B* **365**, 362–366 (2015).
6. Berdova, M. *et al.* Hardness, elastic modulus, and wear resistance of hafnium oxide-based films grown by atomic layer deposition. *J. Vac. Sci. Technol. A* **34**, 051510 (2016).
7. Zhang, Y. *et al.* Patternable Process-Induced Strain in 2D Monolayers and Heterobilayers. *ACS Nano* **18**, 4205–4215 (2024).
8. Gong, L. *et al.* Interfacial stress transfer in a graphene monolayer nanocomposite. *Adv. Mater.* **22**, 2694–2697 (2010).
9. Guo, G. & Zhu, Y. Cohesive-Shear-Lag Modeling of Interfacial Stress Transfer between a Monolayer Graphene and a Polymer Substrate. *J. Appl. Mech.* **82**, 031005 (2015).
10. Cox, H. L. The elasticity and strength of paper and other fibrous materials. *Br. J. Appl. Phys.* **3**, 72–79 (1952).
11. Bronsgeest, M. S. *et al.* Strain Relaxation in CVD Graphene: Wrinkling with Shear Lag. *Nano Lett.* **15**, 5098–5104 (2015).
12. Wang, F. *et al.* Strain engineering in monolayer WS$_2$ and WS$_2$ nanocomposites. *2D Mater.* **7**, 045022 (2020).
13. Jiang, T., Huang, R. & Zhu, Y. Interfacial sliding and buckling of monolayer graphene on a stretchable substrate. *Adv. Funct. Mater.* **24**, 396–402 (2014).
14. Dai, Z., Lu, N., Liechti, K. M. & Huang, R. Mechanics at the interfaces of 2D materials: Challenges and opportunities. *Curr. Opin. Solid State Mater. Sci.* **24**, 100837 (2020).
15. Dorow, C. *et al.* Advancing Monolayer 2-D nMOS and pMOS Transistor Integration from Growth to Van der Waals Interface Engineering for Ultimate CMOS Scaling. *IEEE Trans. Electron Devices* **68**, 6592–6598 (2021).
16. Lin, D. *et al.* Scaling synthetic WS$_2$ dual-gate MOS devices towards sub-nm CET. in *2021 Symposium on VLSI Technology* vol. 1 1–2 (2021).
17. Lin, D. *et al.* Dual gate synthetic WS$_2$ MOSFETs with 120μS/μm Gm 2.7μF/cm^2 capacitance and ambipolar channel. in *2020 IEEE International Electron Devices Meeting (IEDM)* 3.6.1-3.6.4 (IEEE, 2020). doi:10.1109/IEDM13553.2020.9372055.
18. Pang, C. S., Wu, P., Appenzeller, J. & Chen, Z. Thickness-Dependent Study of High-Performance WS$_2$-FETs with Ultrascaled Channel Lengths. *IEEE Trans. Electron Devices* **68**, 2123–2129 (2021).

19. Jin, L. & Koester, S. J. Contact Gating in Dual-Gated WS$_2$ MOSFETs with Semi-Metallic Bi Contacts. *IEEE Electron Device Lett.* **43**, 1575–1578 (2022).

20. Li, M.-Y. *et al.* Wafer-Scale Bi-Assisted Semi-Auto Dry Transfer and Fabrication of High-Performance Monolayer CVD WS$_2$ Transistor. in *2022 IEEE Symposium on VLSI Technology and Circuits (VLSI Technology and Circuits)* 290–291 (IEEE, 2022).

21. Wan, Y. *et al.* Low-defect-density WS$_2$ by hydroxide vapor phase deposition. *Nat. Commun.* **13**, 4149 (2022).

22. Shi, X. *et al.* Improved Self-Heating in Short-Channel Monolayer WS$_2$ Transistors with High-Thermal Conductivity BeO Dielectrics. *Nano Lett.* **22**, 7667–7673 (2022).

23. Sun, Z. *et al.* Statistical Assessment of High-Performance Scaled Double-Gate Transistors from Monolayer WS$_2$. *ACS Nano* **16**, 14942–14950 (2022).

24. Shi, X. *et al.* Ultrashort channel chemical vapor deposited bilayer WS$_2$ field-effect transistors. *Appl. Phys. Rev.* **10**, 011405 (2023).

25. Li, X. *et al.* Rhombohedral-stacked bilayer transition metal dichalcogenides for high-performance atomically thin CMOS devices. *Sci. Adv.* **9**, eade5706 (2023).

26. Sebastian, A., Pendurthi, R., Choudhury, T. H., Redwing, J. M. & Das, S. Benchmarking monolayer MoS$_2$ and WS$_2$ field-effect transistors. *Nat. Commun.* **12**, 693 (2021).

27. Chubarov, M. *et al.* Wafer-Scale Epitaxial Growth of Unidirectional WS$_2$ Monolayers on Sapphire. *ACS Nano* **15**, 2532–2541 (2021).

28. Shen, P.-C. *et al.* Ultralow contact resistance between semimetal and monolayer semiconductors. *Nature* **593**, 211–217 (2021).

29. Schranghamer, T. F. *et al.* Ultrascaled Contacts to Monolayer MoS$_2$ Field Effect Transistors. *Nano Lett.* **23**, 3426–3434 (2023).

30. Das, S., Chen, H. Y., Penumatcha, A. V. & Appenzeller, J. High performance multilayer MoS$_2$ transistors with scandium contacts. *Nano Lett.* **13**, 100–105 (2013).

31. Fitzpatrick, M. E., Fry, A. T. & Holdway, P. *Determination of residual stresses by x-ray diffraction.* (2005).

32. Cverna, F. *ASM ready reference: thermal properties of metals.* vol. 831 (ASM International, 1998).

33. Nix, W. D. Metallic thin films: Stresses and mechanical properties. in *Metallic Films for Electronic, Optical and Magnetic Applications.* 353–421 (Woodhead Publishing, 2014).

34. Yu, H. Z. & Thompson, C. V. Grain growth and complex stress evolution during Volmer-Weber growth of polycrystalline thin films. *Acta Mater.* **67**, 189–198 (2014).

35. Giannozzi, P. *et al.* Quantum ESPRESSO toward the exascale. *J. Chem. Phys.* **152**, 154105 (2020).

36. Schlipf, M. & Gygi, F. Optimization algorithm for the generation of ONCV pseudopotentials. *Comput. Phys. Commun.* **196**, 36–44 (2015).

37. Scherpelz, P., Govoni, M., Hamada, I. & Galli, G. Implementation and Validation of Fully Relativistic GW Calculations: Spin-Orbit Coupling in Molecules, Nanocrystals, and Solids. *J. Chem. Theory Comput.* **12**, 3523–3544 (2016).

38. Yang, J. A. *et al.* Biaxial Tensile Strain Enhances Electron Mobility of Monolayer Transition Metal Dichalcogenides. *ACS Nano* **18**, 18151–18159 (2024).

39. Peña, T. *et al.* Strain engineering 2D MoS$_2$ with thin film stress capping layers. *2D Mater.* **8**, 045001 (2021).

40. Jaikissoon, M., Pop, E. & Saraswat, K. C. Strain Induced by Evaporated-Metal Contacts on Monolayer MoS$_2$ Transistors. *IEEE Electron Device Lett.* **45**, 1528–1531 (2024).